

1 **An automatic lake-model application using near real-time data**
2 **forcing: Development of an operational forecast workflow**
3 **(COASTLINES) for Lake Erie**

4 Shuqi Lin¹, Leon Boegman¹, Shiliang Shan², Ryan Mulligan¹

5 ¹Department of Civil Engineering, Queen's University, Kingston ON Canada K7L 3N6

6 ²Department of Physics and Space Science, Royal Military College of Canada, Kingston ON Canada K7K 7B4.

7 *Correspondence to:* Shuqi Lin (shuqi.lin@queensu.ca)

8 **Abstract.** For enhanced public safety and water resource management, a three-dimensional operational lake
9 hydrodynamic forecasting system COASTLINES (Canadian cOASTal and Lake forecastINg modEl System) was
10 developed. The modelling system is built upon the Aquatic Ecosystem Model (AEM3D) model, with predictive
11 simulation capabilities developed and tested for a large lake (i.e., Lake Erie). The open-access workflow derives
12 model forcing, code execution, post-processing, and web-based visualization of the model outputs, including water
13 level elevations and temperatures, in near real-time. COASTLINES also generates 240-h predictions using
14 atmospheric forcing from 15 km and 25 km horizontal-resolution operational meteorological products from the
15 Environment Canada Global Deterministic Forecast System (GDPS). Simulated water levels were validated against
16 observations from 6 gauge stations, with model error increasing with forecast horizon. Satellite images and lake
17 buoys were used to validate forecast lake surface temperature and the water column thermal stratification. The
18 forecast lake surface temperature is as accurate as hindcasts, with a root-mean-square-deviation <2°C.
19 COASTLINES predicted storm-surges and up-/down-welling events that are important for coastal flooding and
20 drinking water/fishery management, respectively. Model forecasts are available in real-time at
21 <https://coastlines.engineering.queensu.ca/>. This study provides an example of the successful development of an
22 operational forecasting workflow, entirely driven by open-access data, that may be easily adapted to simulate
23 aquatic systems or to drive other computational models, as required for management and public safety.

24 1 Introduction

25 Lakes hold a large proportion of the global surface freshwater, which supports biodiversity and supplies water
26 resources for drinking, transportation, and recreation. However, anthropogenic stressors are causing significant
27 changes in the properties of lakes, such as rapid warming of surface water (O'Reilly et al., 2015), large seasonal
28 water level fluctuations (Gronewold and Rood, 2019), increased frequency of extreme events (Saber et al., 2020)
29 and severe water quality issues such as oxygen depletion (Rowe et al., 2019; Scavia et al., 2014) harmful algal
30 blooms (Brookes and Carey, 2011; Watson et al., 2016). Effort has focussed on investigating the long-term
31 responses of physical processes in lakes to climate change (O'Reilly et al., 2015; Woolway and Merchant, 2019;
32 Jabbari et al., 2021), but improving lake monitoring and developing short-term forecast models, to predict the
33 occurrence of extreme events is also necessary (Woolway et al., 2020). The biogeochemical cycles in lakes are
34 complex and often regulated by physical forcing; therefore, the first step to model and forecast water quality issues,
35 such as harmful algal blooms (Paerl and Paul, 2012; O'Neil et al., 2012) and hypoxia (Rao et al., 2008; Rao et al.,
36 2014) is the development of accurate hydrodynamic models.

37 Over the past several decades, many computer models have been applied to hindcast (running models
38 forced with and validated against historically collected data) lake hydrodynamics to aid management. These range
39 from one-dimensional (1D) models such as DYRESM (Antenucci and Imerito, 2000), Simstrat (Gaudard et al.,
40 2017), and GLM (Hipsey et al., 2014), to three-dimensional (3D) models such as Delft3D (Lesser et al., 2004),
41 FVCOM (Chen et al., 2012; Rowe et al., 2019) ELCOM (Hodges et al., 2000). Several of these hydrodynamic
42 models may be coupled to biogeochemical models to allow for prediction of water quality. In the case of hindcast
43 applications, the complex and time-consuming setup and calibration procedure, of these models, can result in a
44 significant time lag (months to years) between when a project is initiated and when the model results are
45 communicated to stakeholders. This delay severely limits the utility of computational models for policy and
46 management decision making. For better application of these powerful computational tools, the ability for rapid
47 monitoring and simulation forecasts should be established.

48 In addition to the significant effort required to setup and calibrate models, other hurdles exist such as data-
49 sharing agreements between the agencies collecting forcing/validation data and those running the models. For
50 example, the US National Oceanic and Atmospheric Administration (NOAA) Great Lakes Coastal Forecasting
51 System (Chu et al., 2011; Anderson et al., 2018), is a comparatively large-budget multi-institutional (NOAA-
52 GLERL and U. Michigan-CIGLR) project that predicts water levels, temperature profiles, currents, and wave
53 heights over a 120-h timeframe in the five Laurentian Great Lakes and connecting channels, using FVCOM on a 3D
54 unstructured grid with 30-2000 m horizontal resolution. Similarly, meteolakes.ch (Baracchini et al., 2020b) applies
55 Delft3D for short-term 3D forecasts (4.5 days) of four Swiss lakes and simstrat.eawag.ch (Gaudard et al., 2019)
56 applies Simstrat for near-realtime 1D simulation of 54 Swiss lakes. These latter applications employ a data sharing
57 agreement between Swiss Federal Institute of Aquatic Science and Technology (EAWAG), École Polytechnique
58 Fédérale de Lausanne (EPFL) and MeteoSwiss.

59 Owing to the present online proliferation of near real-time lake observation data (e.g., National Data Buoy
60 Center (NDBC; <https://www.ndbc.noaa.gov/>); Great Lakes Observation System (GLOS; <https://www.glos.us/>)) and

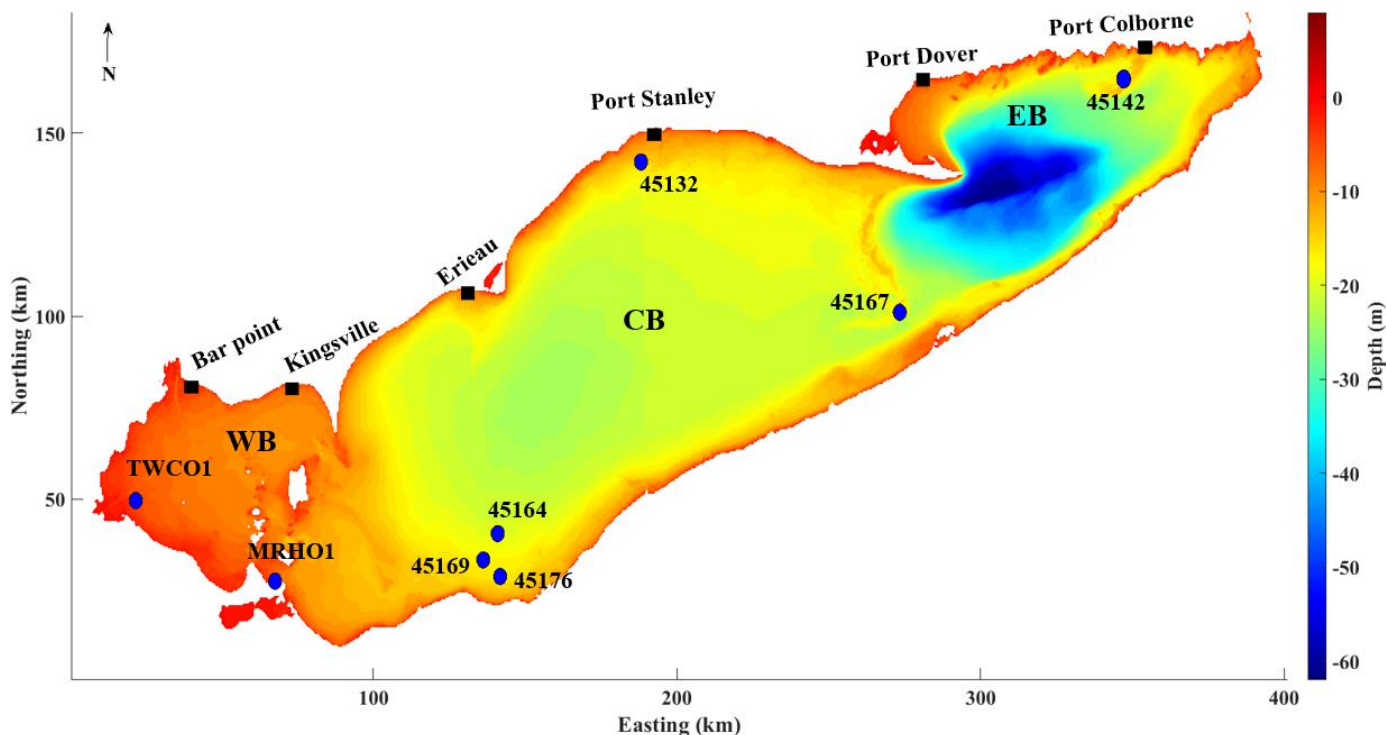
61 high-resolution meteorological forecasts (e.g., Global Deterministic Prediction System, GDPS;
62 https://dd.weather.gc.ca/model_gem_global/; High Resolution Rapid Refresh, HRRR;
63 <https://rapidrefresh.noaa.gov/hrrr/>) the data-sharing agreements and managed data transfer protocols are no longer
64 required. When coupled with recent dramatic improvements in workflow efficiency (e.g., Gaudard et al. (2019);
65 Baracchini et al. (2020b)) near real-time inclusion of forcing from meteorological forecasts allow for the
66 development of specific simulations tailored to meet diverse lake-management needs (e.g., prediction of coastal
67 flooding, spill modelling, fish habitat, beach closures, and optimization of treatment or source water monitoring
68 strategies).

69 In the present study we developed and tested the COASTLINES (Canadian cOASTal and Lake forecastINg
70 modEl System; <https://coastlines.engineering.queensu.ca/>) lake-model application workflow, that rapidly accesses
71 near real-time online data (weather forecasts, water level and temperature observations) for automated model
72 forcing, execution and validation. Hydrodynamic forecasts are automatically post-processed and posted on a web
73 platform. We provide an overview of the COASTLINES system, including model implementation for Lake Erie
74 (Section 2 Data and methods) and the accuracy of COASTLINES in forecasting water levels and temperature fields
75 over timescales of 24-h and 240-h (Section 3 Results). In Section 4 Discussion, the predictive ability of
76 COASTLINES for decision making is showcased through prediction of hydrodynamic events associated with fish
77 kills, hypoxia near a drinking water intake and coastal flooding from a storm surge. We also discuss the relative
78 advantages of COASTLINES in comparison to other model products, including bias and uncertainty.

79 **2 Data and methods**

80 **2.1 Study site**

81 Lake Erie, the shallowest lake of the Great Lakes with a mean depth of 19 m. Lake-wide hydrodynamics
82 predominantly exhibits free surface and current oscillations from the 14-h barotropic seiche (Hamblin, 1987;
83 Boegman et al., 2001). The lake morphometry consists of distinct, yet interconnected western, central, and eastern
84 basins (Fig. 1), each with its own water quality concerns: The 11-m deep western basin is typically well mixed and
85 has frequent harmful algae blooms related to climate-driven meteorological forcing (Michalak et al., 2013). The
86 ephemeral stratification in late summer (Loewen et al., 2007) regulates vertical biogeochemical fluxes (Boegman et
87 al., 2008). The 20-m deep central basin is prone to large-scale hypolimnetic hypoxia (Scavia et al., 2014).
88 Hydrodynamics are governed by an internal Poincaré wave (Bouffard et al., 2012; Valipour et al., 2015) and a bowl-
89 shaped depression of the summer thermocline, which influence the oxygen budget (Beletsky et al., 2012; Bouffard et
90 al., 2014). The 65-m deep eastern basin has nearshore water quality concerns from *cladophora* (Higgins et al., 2006)
91 and ecosystem engineering by dreissenid mussels (Hecky et al., 2004). Hydrodynamics of this region are controlled
92 by the coastal internal Kelvin wave (Valipour et al., 2019).



94 **Fig.1 Map of Lake Erie showing the bathymetric depths and observation sites. The bathymetric map is at the**
 95 **resolution of the 500 m grid applied in the model. The western, central, and eastern basins are labeled as WB,**
 96 **CB, and EB, respectively. Blue circles indicate lake buoys and black squares indicate water level gauges.**

97 2.2 Model description

98 COASTLINES applies the three-dimensional Aquatic Ecosystem Model (AEM3D, version 1.1.1, HydroNumerics
 99 Pty Ltd.). This model solves the unsteady 3D Reynolds-averaged Navier-Stokes equations for incompressible flow
 100 employing the Boussinesq and hydrostatic approximations. Momentum advection is based on the Euler-Lagrange
 101 method with a conjugate-gradient solution for the free-surface height (Casulli and Cheng, 1992), and a conservative
 102 ULTIMATE QUICKEST discretization scheme for advection of scalars (Leonard, 1991). AEM3D is a parallel
 103 version of the commonly applied Estuary and Lake Computer Model (ELCOM; (Hodges et al., 2000). ELCOM has
 104 been applied to Lake Erie to simulate currents and seasonal circulation (León et al., 2005), the internal Poincaré
 105 (Valipour et al., 2015) and Kelvin waves (Valipour et al., 2019), ice cover (Oveisy et al., 2012) and the response of
 106 the thermal structure, in Lake Erie, to air temperature and wind speed changes (Liu et al., 2014). ELCOM has been
 107 coupled with the biogeochemical CAEDYM model to simulate Lake Erie phytoplankton and nutrients (León et al.,
 108 2011), and the response of hypoxia (Bocaniov and Scavia, 2016) and algae blooms (Scavia et al., 2016) to nutrient
 109 load reductions. Recent applications of AEM3D include a study of the water level in Lake Arrowhead, California
 110 (Saber et al., 2020), ice cover in Lake Constance (Caramatti et al., 2019) and pollutant transport in Lake St. Clair
 111 (Madani et al., 2020).

112 2.3 Model setup and meteorological forcing variables

113 To adequately resolve the coastal boundary layer (~ 3 km width (Rao and Murthy, 2001)) and basin-scale internal
114 waves (Poincaré (16.8 h) and Kelvin waves), the bathymetry of Lake Erie
115 (<https://www.ngdc.noaa.gov/mgg/greatlakes/erie.html>) was discretized into a 500 m × 500 m horizontal grid, which
116 is ~10 % of the internal Rossby radius (Schwab and Beletsky, 1998). The lake was discretized into 45 vertical
117 layers, with fine resolution (0.5 m) through the surface layer, metalimnion and bottom of the central basin, and
118 coarse layers (5 m) through the hypolimnion of the deeper eastern basin to the maximum depth of 64 m.
119 The model was ‘cold started’ on April 8, 2020 (day of year (day) 99) with an initial temperature field spatially
120 interpolated from observed water temperatures at stations 45142 and MHRO1; a time when spring turnover causes
121 thermal stratification to be minimal. The model time step is $dt = 300$ s to satisfy the $CFL = \sqrt{2}$ (Courant-Friedrichs-
122 Lewy) condition for internal waves (Hodges et al., 2000).

123 The model is forced by the surface meteorology (wind speed, wind direction, air temperature, shortwave
124 solar radiation, relative humidity, air pressure, and net longwave radiation), with net longwave radiation being
125 computed internally within AEM3D from cloud cover and the modelled surface temperature. In order to address the
126 spatial variability of meteorological conditions across the lake, the computational domain was forced with
127 meteorological data on horizontal grids at 15 km (https://dd.weather.gc.ca/model_gem_global/15km/) and 25 km
128 (https://dd.weather.gc.ca/model_gem_global/25km/) resolution using meteorological forecasts from the
129 Environment and Climate Change Canada Global Deterministic Forecast System (GDPS). This resulted in 31 and 23
130 meteorological sections for the 15 km and 25 km models, respectively. Wind speed, wind direction, air temperature,
131 relative humidity, air pressure, dew point, and cloud cover are direct outputs from GDPS, with solar radiation
132 calculated based on dew point and air pressure ((Meyers and Dale, 1983); Appendix C. in (Gaudard et al., 2019)).
133 The meteorological forecast has an output timestep of 3-h and a forecast length of 240 h. The .GRIB2
134 meteorological data were retrieved with the ‘urllib’ library in Python and formatted into AEM3D input files using
135 the nctoolbox in MATLAB.

136 In this pilot application, the Lake Erie inflows and outflows, which roughly balance, are neglected,
137 however evaporation and precipitation are accounted for in the water balance. Over short timescales (<10 days), the
138 contributions from evaporation and precipitation to water level change are minor, with water level oscillations
139 resulting from storm surges and surface seiches (Treibitz, 2006).

140 2.4 Observations, implementation, and model validation

141 The water levels and temperatures simulated by COASTLINES were validated using both in situ and satellite
142 observations. Near real-time water level data was used from six stations along the Canadian coastline, which
143 reported hourly observations (Bar Point, Kingsville, Erieau, Port Stanley, Port Dover, and Port Colborne; Fig. 1;
144 Table 1), retrieved from Fisheries and Oceans Canada (<https://marees.gc.ca/eng/find/zone/44>). The data are parsed
145 using the ‘BeautifulSoup’ library in Python and saved as .csv files, to be read with MATLAB for model validation.
146 The observations showed higher fluctuations in the western (Bar Point and Kingsville) and eastern (Port Dover and

147 Port Colborne) basins (Fig. 1). Thus, we quantify the water level forecast capability and uncertainty in terms of the
148 Root Mean Square Deviation (RMSD) and Relative Error (RE):

$$149 \quad RMSD = \left[\frac{1}{N} \sum_{i=1}^N (x_i - y_i)^2 \right]^{1/2}, \quad (1)$$

$$150 \quad RE = 100 \frac{RMSD}{\log. \text{mean}(\text{daily range})}, \quad (2)$$

151 where x_i and y_i ($i = 1, 2, 3, \dots, N$) are the model and observed water level timeseries and N is the number of samples.
152 RMSD is the absolute error of the model against the observation. The difference between the observed daily
153 minimum and maximum value was defined as the daily water level fluctuation range, where RE is the ratio between
154 the RMSD and lognormal mean of daily range over April to September 2020. Given that our study focusses on a
155 240-h forecast, RE can characterize the forecast bias, regardless of the instantaneous water level position. Here,
156 forecast uncertainty is in the evaluation statistic from combining forecast dates – not actual uncertainty in an
157 individual forecast.

158 Eight in situ lake buoys, distributed over the nearshore areas of the three basins (Fig. 1; Table 1), provided
159 near real-time model validation data through the Great Lakes Observing System (GLOS: <https://www.glos.us/>) and
160 National Data Buoy Center (NDBC: <https://www.ndbc.noaa.gov/>) portals. For each station, the text-based NDBC
161 observations are parsed using the ‘BeautifulSoup’ Python library, and the GLOS observations are retrieved using
162 ‘webdriver’ from the ‘selenium’ Python library. All the lake buoy observations are saved as .csv files and read into
163 MATLAB for post-processing. Attempts to retrieve missing variables would result in run-time errors.

164 The lake buoys are deployed from April or May through mid-October, spanning the spring/fall turnover
165 and seasonal summer stratification periods. However, due to COVID-19 related delays in instrument deployments in
166 2020, only two buoys located offshore of Cleveland, near the water intake crib (station 45176 and station 45164),
167 were equipped with thermistor chains to monitor temperature profiles. The other six buoys provide air and lake
168 surface temperature as well as wind speed and direction observations for hydrodynamic and meteorological forecast
169 validation. Satellite-based observations of lake surface temperature were obtained from the Great Lakes Surface
170 Environmental Analysis (GLSEA2), which is derived from NOAA CoastWatch AVHRR (Advanced Very High-
171 Resolution Radiometer) imagery and updated on NOAA GLERL website
172 (https://coastwatch.glerl.noaa.gov/erddap/files/GLSEA_GCS/). GLSEA2 produced daily observations, with 2.6 km
173 resolution, from the cloud-free portions of the satellite images (Schwab et al., 1999). The netCDF data are retrieved
174 using the ‘BeautifulSoup’ library and ‘webdriver’ from ‘selenium’.

175 We quantified the temperature forecast capability using the statistical measures of RMSD (eq. 1) and Mean
176 Bias Deviation (MBD):

$$177 \quad MBD = 100 \frac{\frac{1}{N} \sum_{i=1}^N (x_i - y_i)}{\frac{1}{N} \sum_{i=1}^N y_i} \quad (3)$$

178 For the spatial MBD and RMSD (s-MBD and s-RMSD), x_i and y_i are the model and observed temperature in each
179 grid, and N is the total number of grids. For timeseries MBD and RMSD (t-MBD and t-RMSD), x_i and y_i are the
180 model and observed temperature at each sample time, and N is the total number of samples.

181
182
183
184

Table 1
Details of field stations with water level gauges and lake buoys.

Station	Parameter	Sampling interval (min)	Depth of measurement (m)
Bar Point	Water level	60	Surface
Kingsville	Water level	60	Surface
Erieau	Water level	60	Surface
Port Stanley	Water level	60	Surface
Port Dover	Water level	60	Surface
Port Colborne	Water level	60	Surface
TWCO1	Temperature	10	Surface
45005	Temperature	10	Surface
45176	Temperature	10	1, 3, 4, 6, 7, 9, 10, 12, 14, 15
45169	Temperature	30	surface
45164	Temperature	60	1, 2, 4, 6, 8 10
45132	Temperature	60	Surface
45167	Temperature	10	Surface
45142	Temperature	60	Surface

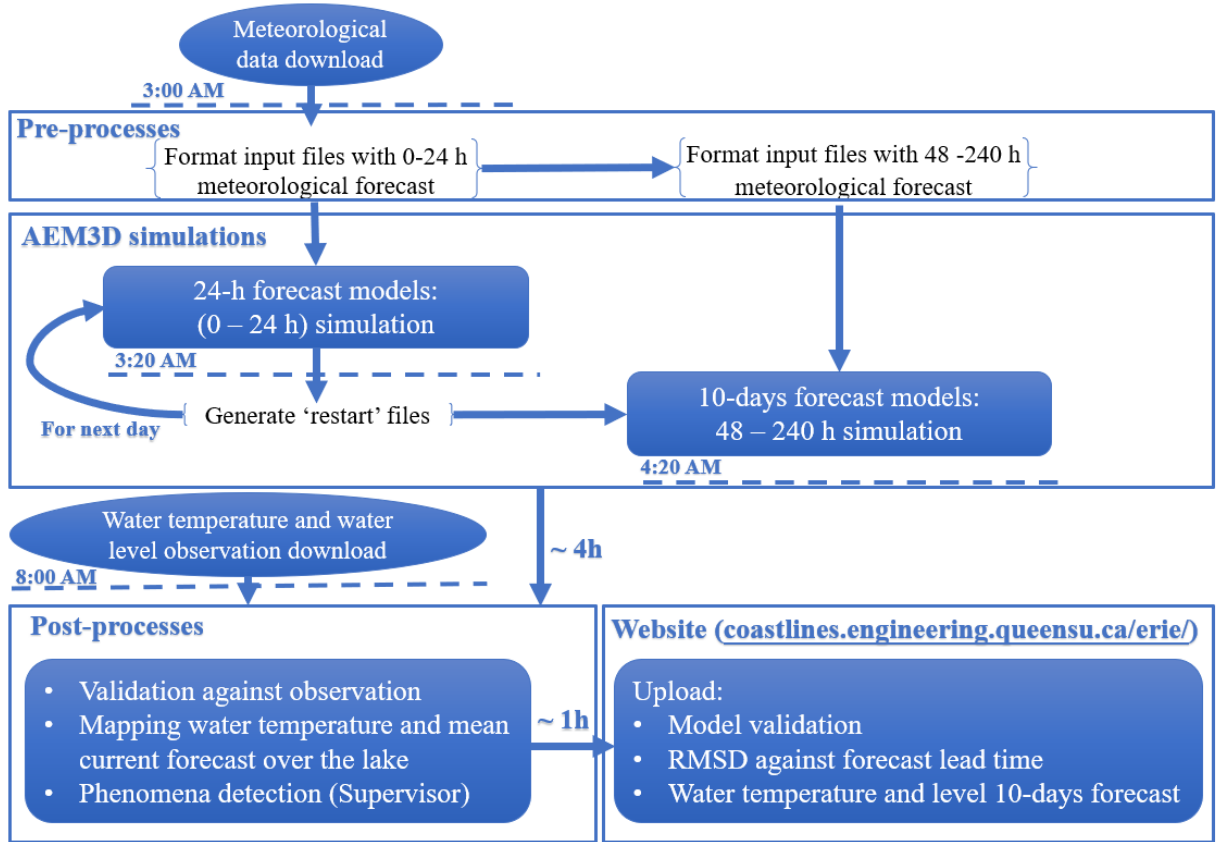
185 **2.5 System operation**

186 The COASTLINES operational forecast system is run on a local server supported by Queen’s University ITS
187 (Kingston, Canada). The COASTLINES workflow is presented in Fig. 2. The system consists of input data
188 acquisition and preparation, 24-h hydrodynamic simulations, 240-h hydrodynamic simulations, validation against in
189 situ observations, and uploading the model forecasts and validation to the web platform. Given that the standard
190 deviations of meteorological forecast variables increase with forecast lead time (Buehner et al., 2015), we performed
191 separate 24-h and 240-h forecast simulations each day. The model advances every day according to the 24-h forecast
192 simulation and terminates by generating ‘re-start’ files. These files are then used to hot-start the 240-h forecast
193 simulation and the 24-h simulations for the next day. The input files for the 240-h forecast simulations are
194 iteratively replaced by the new 240-h meteorological forecast generated each day. The 24-h and 240-h forecast
195 model outputs are compared against observations to evaluate the forecast performance against forecast lead time.

196 The long-term stability of employing daily ‘hot’ restarts can be seen in a comparison between simulated
197 temperature profiles from a continuous run and that from stitching together the 24-h hot-start simulations (Appendix
198 A; Fig. A1). At present, the initial water level cannot be modified using the AEM3D re-start files. Therefore, to
199 account for long term drift in surface water level, we used real time gauge observations as the datum point for water
200 level forecasts (automatically performed by MATLAB in post processing) and only consider errors resulting from
201 simulation of storm surges and seiches, as opposed to those from seasonal changes in mean lake level. Automation
202 of the processing tasks in the workflow is performed by Python scripts triggered by the Windows Task Scheduler
203 every 24-h at midnight. The online meteorological forecast data are retrieved from GDPS once updated at 3 am
204 EST. Forcing variables are then formatted in MATLAB, called by the Python scripts once the meteorological
205 forecast data has been retrieved. The AEM3D pre-compiled executable is then run as a black-box code, triggered by
206 Python. The 24-h and 240-h simulations take 0.5 h and 4 h to complete, respectively. The observed data, including
207 water levels from gauge stations, water temperatures from lake buoys and satellite images are scraped with Python

208 at 8 am, followed by post-processing in MATLAB to validate model output, calculate statistical metrics (RMSD,
 209 MBD) and generate figures. The results are exported to Google sheets and published to the COASTLINES website
 210 (e.g., Appendix B). The authors (supervisors of COASTLINES) and Queen’s ITS monitor forecast results and
 211 maintain system operation.

212 Global coverage of the GDPS forecasts enable this operational system to be readily implemented at other
 213 sites where lake bathymetry, boundary flows and in-situ validation data are available. The workflow may be easily
 214 modified to include additional meteorological forecasts or other black-box hydrodynamic drivers (e.g., HRRR and
 215 Delft3D, respectively (Rey and Mulligan, 2021)). This would require simple modification of the COASTLINES
 216 MATLAB-based write statements to meet the formatting requirements of a particular driver.



217
 218 **Fig. 2 Daily workflow and automated processes in the COASTLINES operational system as performed on the**
 219 **local server.**

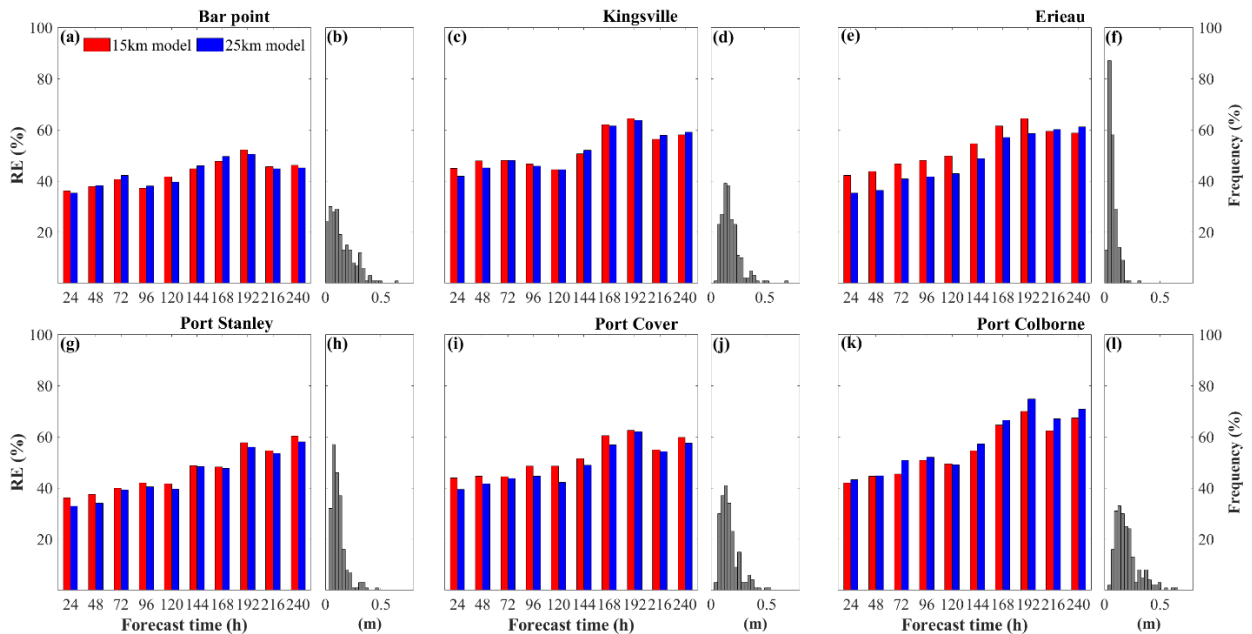
220 **3 Results**

221 The COASTLINES water level and temperature forecasts have been operational since April and July 2020,
 222 respectively. The 24-h and 240-h forecast water levels from the 15 km and 25 km resolution models were validated
 223 against real-time gauge station observations. The water level statistical metrics (RMSD and RE) were averaged over
 224 April to September 2020. The 24-h and the 240-h forecast lake surface temperature and temperature profiles, from

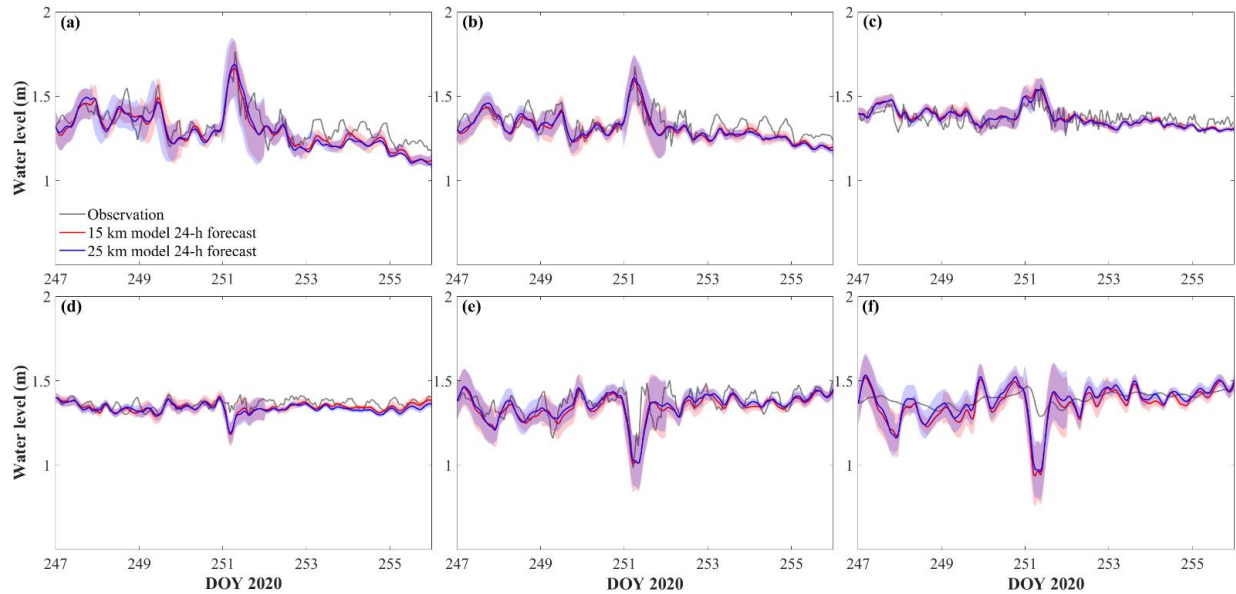
225 the models, were also validated against real-time lake buoy data and daily averaged satellite imagery. The timeseries
 226 and spatial MBD and RMSD (t-RMSD, t-MBD and s-RMSD, s-MBD) were averaged over July to September 2020.

227 **3.1 Water level**

228 The Relative Error (RE) of the forecast water level increases with forecast time when averaged over April to
 229 September 2020; the 24-h forecast error being ~ 40% at all six gauge stations (Fig. 3 a, c, e, g, i, k). Given the large
 230 water level fluctuation at Port Colborne (Fig. 3 l), the 240-h forecast RE is highest at this station, exceeding 70%
 231 (Fig. 3 k). Of the six gauge stations reported in this study, those at the western (Bar Point and Kingsville) and
 232 eastern (Port Dover and Port Colborne) ends of Lake Erie longitudinal axis had the largest water level fluctuations,
 233 resulting from the predominant south-westerly winds generating strong wind set-up and surface seiches (Fig. 3 b, d,
 234 f, h, j, l). The lognormal means of the daily range in water level at the six gauge stations are 0.21 m (Bar Point),
 235 0.16 m (Kingsville), 0.07 m (Erieau), 0.10 m (Port Stanley), 0.15 m (Port Dover), 0.17 m (Port Colborne).
 236 The 24-h forecasts show qualitative agreement with observations in phase and magnitude (Fig. 4). The 24-h
 237 forecasts reproduce the dramatic surface seiches induced by westerly winds $> 15 \text{ m s}^{-1}$ (Fig. C2) on day 251 (RMSD
 238 $< 0.1 \text{ cm}$), especially the obvious water level fluctuations at stations in the western and eastern basins (Fig. 4 a, b, e).
 239 However, the prediction of water level at Bar Point showed large bias (Fig. 4 f), with the model overestimating the
 240 water level fluctuation. The uncertainty in the model forecast, which increased with the range of the daily
 241 fluctuation, was captured by the 24-h forecast RE over April to September (the shaded areas in Fig. 4). Overall, the
 242 confidence interval of the 24-h forecast included most of the discrepancies between the observations and the model
 243 results.



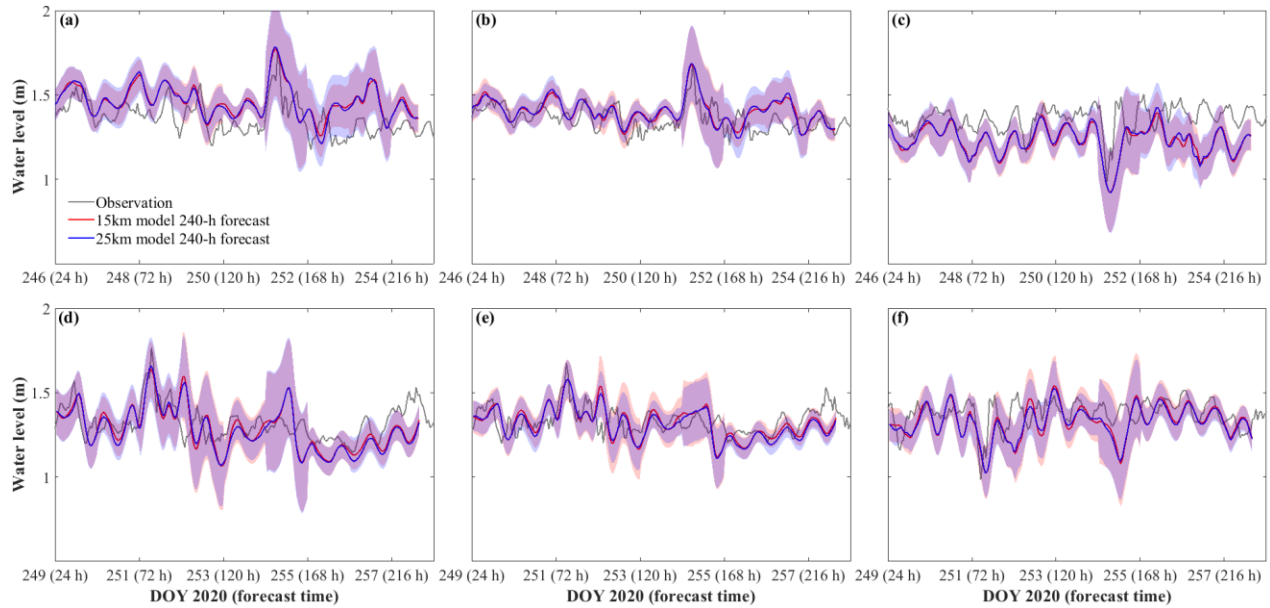
244
 245 **Fig. 3 Relative error (RE) in water level predictions against forecast time at six stations (a, c, e, g, i, k). Panels**
 246 **(b, d, f, h, j, l) are the corresponding frequency distribution of lognormal means of the daily water level**
 247 **fluctuation range (x-axes, unit in meter) at Bar Point, Kingsville, Erieau, Stanley, Port Dover, Port Colborne,**
 248 **respectively.**



249

250 **Fig. 4 Comparison between observed and stitched 24-h forecast modeled water level at (a) Port Colborne, (b)**
 251 **Port Dover, (c) Port Stanley, (d) Erieau, (e) Kingsville, and (f) Bar Point. The shaded areas show the confidence**
 252 **interval of the 15 km model (red shading) and the 25 km model (blue shading), as given by the 24-h RE in Fig.**
 253 **3.**

254 Timeseries validations for the 240-h model forecast (Fig. 5) include confidence intervals from the RE (Fig. 3). As
 255 shown, the forecast began 6 days in advance of the large surface seiche event on day 251 and predicted the seiche to
 256 crest at Port Colborne 1-2 h ahead of the observations, and to trough at Kingsville 1-2 h behind the observations
 257 (Fig. 5 a, c). Damping of the seiche oscillations (~144 hours in the future) was excessive, with the water levels being
 258 underestimated and the phase shifted by approximately 12 hours (Fig. 5. a, b). Despite the wide confidence intervals,
 259 due to the increasing RE with forecast time, large bias existed after the seiche event (forecast time >168 hours).
 260 When the forecast was initiated close to the event (3 days before), the prediction of seiche phase was more accurate
 261 (Fig. 5 d, e, f); however, the seiche decay still had a 12-h phase shift. The discrepancies in seiche amplitude (< 0.1
 262 m) were within the confidence intervals of the models.



263

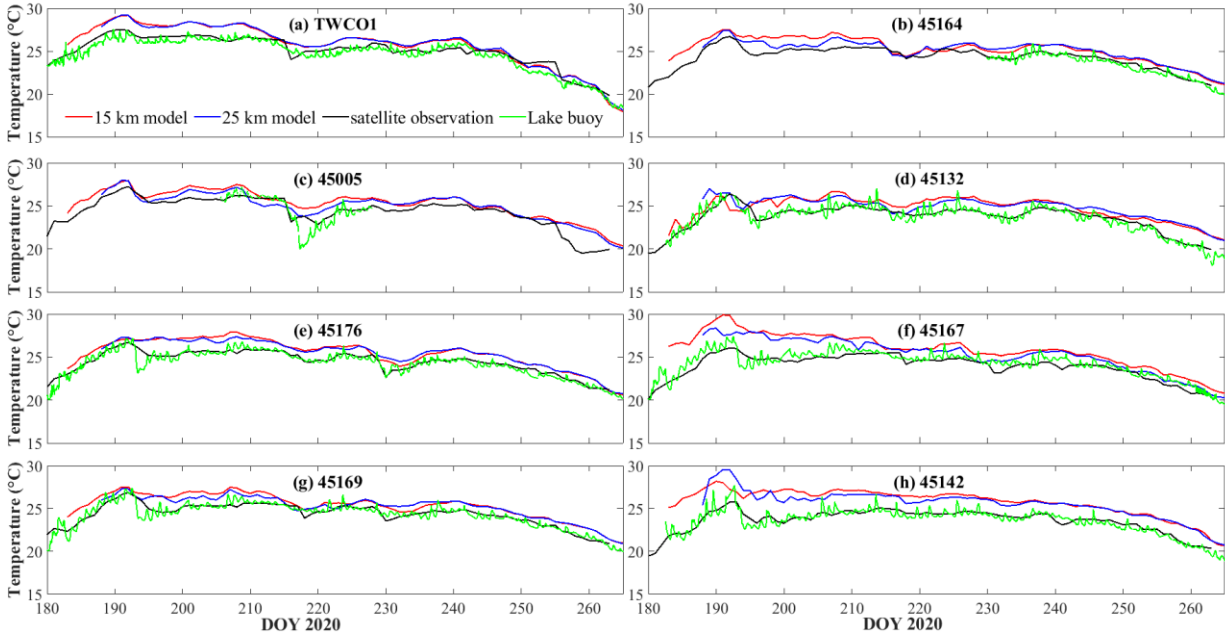
264 **Fig. 5 Comparison between the observed water level and 240-h forecast hot-started on day 245 (a, b, c) and day**
 265 **248 (d, e, f) at Port Colborne, Port Dover, and Kingsville, respectively. The shaded areas show the confidence**
 266 **interval of the 15 km model (red shading) and the 25 km model (blue shading), as given by the 240-h RE in Fig.**
 267 **4.**

268 3.2 Water temperature

269 3.2.1 Lake surface temperature

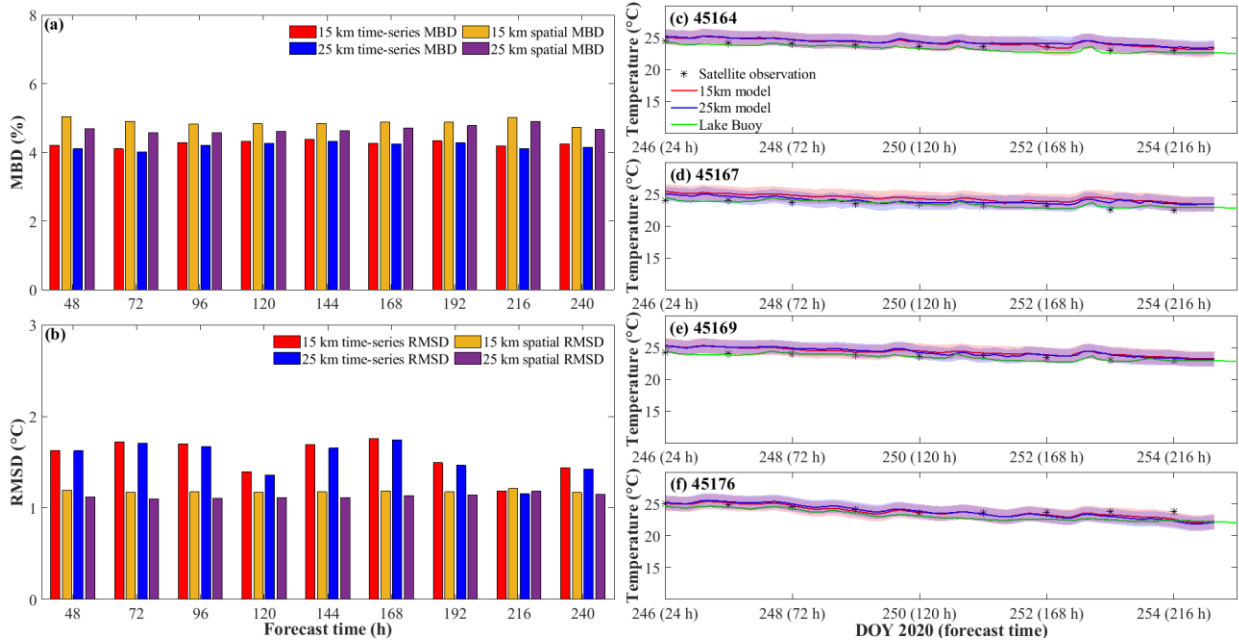
270 Using satellite-based and lake buoy-based observations, we evaluated the lake surface temperature forecast (Fig. 6).
 271 The 24-forecast captured the seasonal variation of lake surface temperature, particularly the rapid increase in
 272 temperature on days 180-190, and the gradual decrease in temperature after day 240; at all eight stations. However,
 273 the forecast overestimated the lake surface temperature in July by 3-5 °C (days 180-210), particularly at STN 45167
 274 and 45142. Due to the 3-h output interval associated with the meteorological forecast data, the forecast model was
 275 insensitive to temperature fluctuations over shorter timescales, as recorded by the lake buoys, and it underestimated
 276 the sudden decrease in temperature near day 220 and 255 at STN 45005.

277 Overall, the t-MBD and t-RMSD, over these eight stations, were ~6% and 1.4 °C (15 km model) and ~5%
 278 1.3 °C (25 km model) for the 24-h forecast, respectively (Table 2). The average s-MBD and s-RMSD over the 50
 279 days from July-September were ~4% and 1.2 °C, respectively, for both 15 km and 25 km resolution models.



280

281 **Fig. 6 Comparison between the stitched 24-h forecast and observed lake surface temperature at 8 stations (a)**
 282 **TWCO1, (b) 45164, (c) 45005, (d) 45132, (e) 45176, (f) 45167, (g) 45169, and (h) 45142. The green lines are**
 283 **timeseries observations from lake buoys, the black lines are daily observations derived from satellite imagery.**



284

285 **Fig. 7 (a) Mean-Bias Deviation (MBD) against forecast time; (b) Root-Mean-Square Deviation (RMSD) against**
 286 **forecast time. (c-f) Timeseries of 240-h forecast and observed lake surface temperature at stations 45164, 45167,**
 287 **45169, 45176, respectively, and daily averaged satellite lake surface temperature (black asterisks). The**
 288 **confidence interval (shaded areas) in (c-f) represents the uncertainty of the 240-h forecast model through the**
 289 **timeseries RMSD with the forecast time (panel b).**

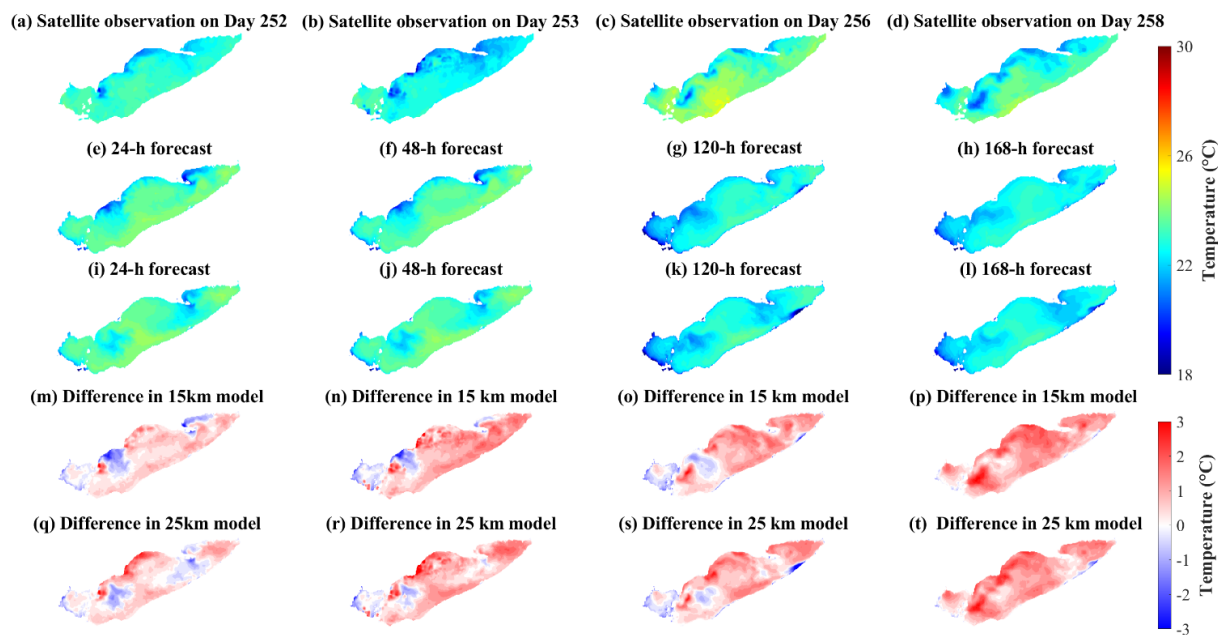
290 The 240-h forecast MBD and RMSD, surprisingly, do not show an increase in error with forecast time (Fig. 7 a, b).

291 Both t-MBD and s-MBD, over the 240-h forecast, are ~4-5%, with s-MBD 0.5-1% higher than t-MBD. Although

292 both 240-h s- and t-RMSD are under 2 °C, the t-RMSD show the error with forecast time to be higher than s-RMSD.
 293 Both timeseries observations from lake buoys and daily averaged observations from satellite imagery fall into the
 294 forecast confidence interval based on the 240-h t-RMSD (Fig 7 c-f).

295 Spatial comparisons of satellite-based observations to the 24-h, 48-h, 120-h, 168-h surface temperature
 296 forecasts illustrate that the forecast system (with 15 km meteorological data) predicted the cooler water mass along
 297 the northwest shoreline of the central basin with a cold bias ~ 2 °C (Fig. 8); this may be up-welling hypolimnetic
 298 water (see following Discussion 4.2). The model also predicted lower surface temperatures in coastal regions of the
 299 western basin with a cold bias ~ 2 °C (Fig. 8 m-t); the bias presumably was induced by neglecting riverine inflows
 300 (e.g., Detroit River and Maumee River; see also Discussion 4.3), which are typically near the air temperature and
 301 several degrees warmer than the lake surface (Wang and Boegman, 2021). Further comparisons between model
 302 predictions and satellite-based observations of lake surface temperature can be found in the Supporting material
 303 (Fig. D1-2).

304



305

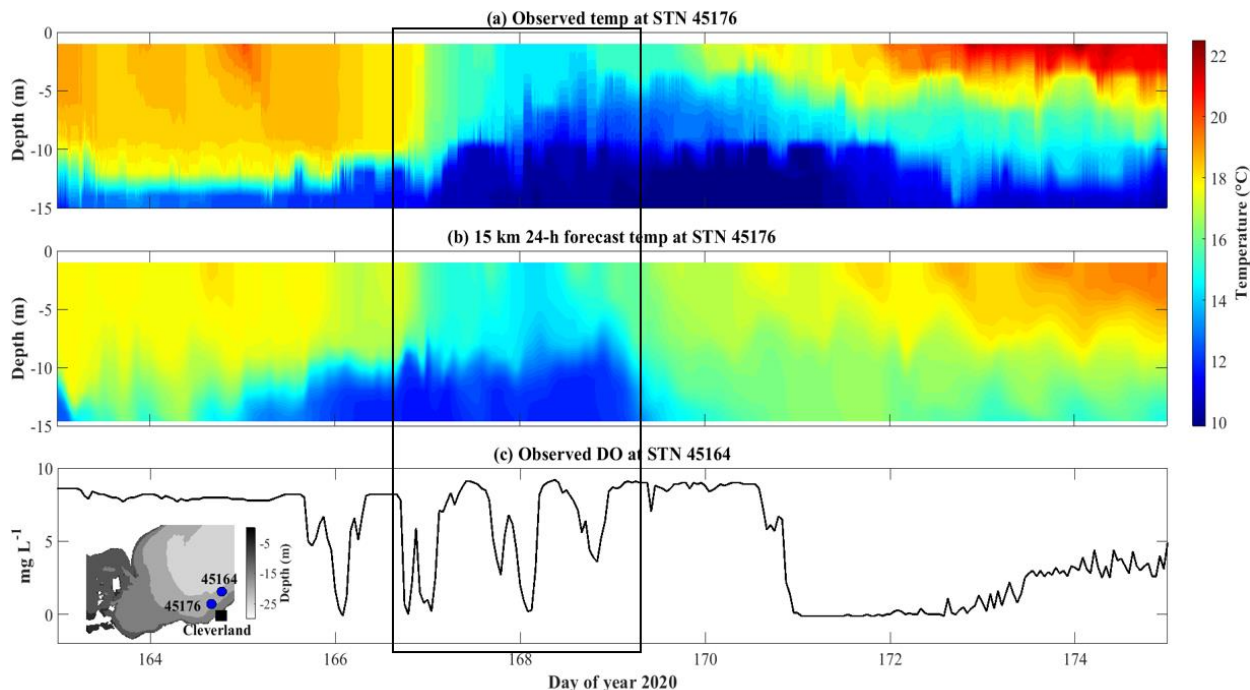
306 **Fig. 8 Comparison of lake surface temperature from (a-d) satellite observations, (e-h) 15 km model forecast,**
 307 **and (i-l) 25 km model forecast during late summer. The models were hot-started on day 251. The difference**
 308 **between observations and models are shown in (m-t).**

309 3.2.2 Thermal structure

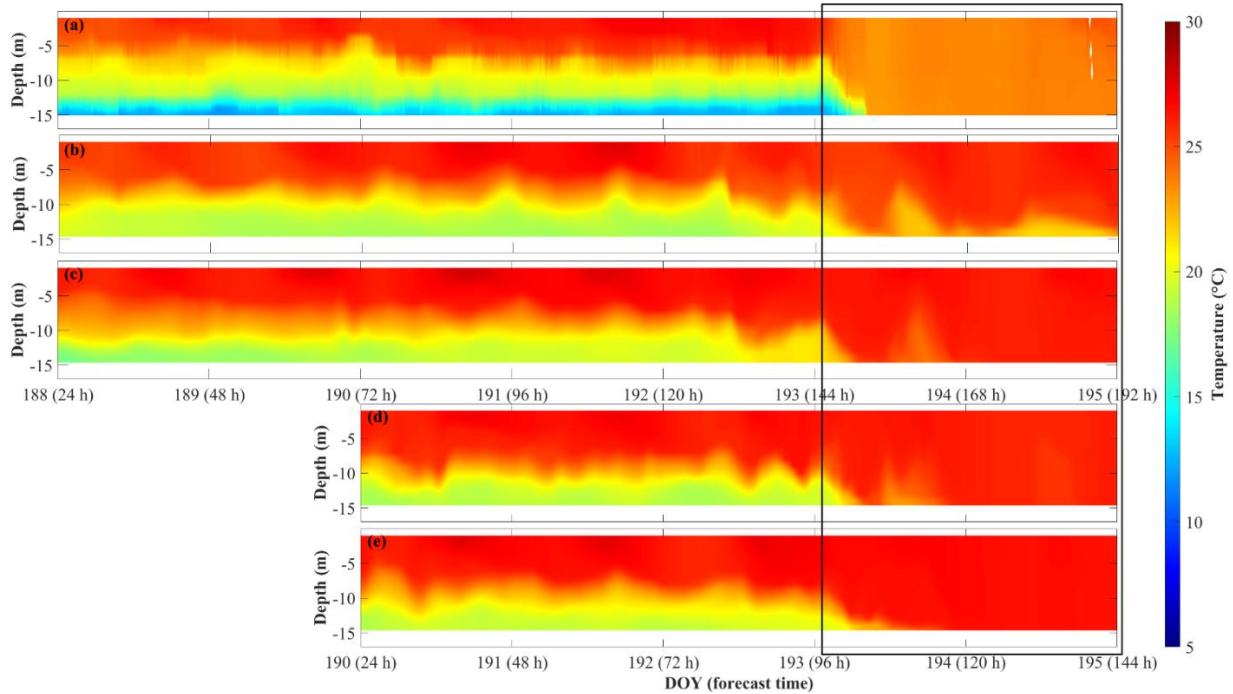
310 The 3D AEM3D model structure applied in COASTLINES enables the prediction of the thermal profiles in the lake.
 311 On 15 Jun. 2020 (day 168), a rapid drop (~ 6 °C) in surface temperature, was recorded by the thermistor at STN 45176,
 312 and predicted by the stitched 24-h COASTLINES model (15 km meteorological input) (Fig. 9 a, b). The timing and
 313 intensity of this up-welling event were accurately forecast, but before and after the upwelling event, the mixed layer
 314 depth was modelled to be deeper than observed; perhaps a result of spurious numerical diffusion resulting from the

315 thermocline swashing along the stair-step z-level grid at the lake perimeter. The 240-h forecast model was not yet
316 operational at this time.

317 Both the 240-h 15 km and 25 km resolution forecasts predicted the down-welling event on 11 Jul. 2020 (day
318 193) at STN 45176 (Fig. 10). The forecasts were hot-started 7 days before the event (day 187), successfully predicting
319 when warm surface water down-welled toward the bed displacing the thermocline (Fig. 10 b, c), but the 15 km
320 resolution underestimated the intensity of down-welling, predicting thermocline recovery on day 193. The forecast
321 hot-started 5 days before the event (day 189) gave a more accurate prediction with the down-welling persisting over
322 2 days (Fig. 10 d, e) – as observed (Fig. 10 a).



323
324 **Fig. 9** Temperature profile comparisons between (a) observations and (b) stitched daily 24-h forecasts from the
325 15 km resolution model at station 45176. (c) Observed dissolved oxygen concentration at station 45164 from
326 lake buoy (<https://www.glos.us/>). The inset image shows the bathymetry and locations of lake buoys. The black
327 square indicates the timing of the up-welling event.



328

329 **Fig. 10** Comparisons of (a) observed temperature profile, (b, d) 240-h 15 km resolution modeled, and (c, e) 240-
 330 h 25 km resolution modeled temperature profiles at STN 45176. The forecast models were hot-started on day
 331 187 (b, c), and day 189 (d, e). The black square indicates the down-welling event.

332 **Table 2**

333 **Statistical measures of t-MBD (Mean-Bias Deviation) and t-RMSD (Root-Mean-Square Deviation) between**
 334 **the 24-h forecast model and observations of water temperature.**

Station	RMSD (°C)		MBD (%)	
	15 km model	25 km model	15 km model	25 km model
45176	2.6	2.6	6.8	6.8
45164	1.8	2.1	2.2	2.3
45132	1.5	1.5	5.5	5.7
45142	2.4	2.1	9.9	8.8
45167	1.2	1.1	4.6	4.0
45169	1.3	1.2	4.7	4.6
TWCO1	1.0	1.0	3	1.9
45005	1.2	1.1	8.2	7.9

335 **4 Discussion**

336 **4.1 Prediction of coastal up-welling for fishery and drinking water management**

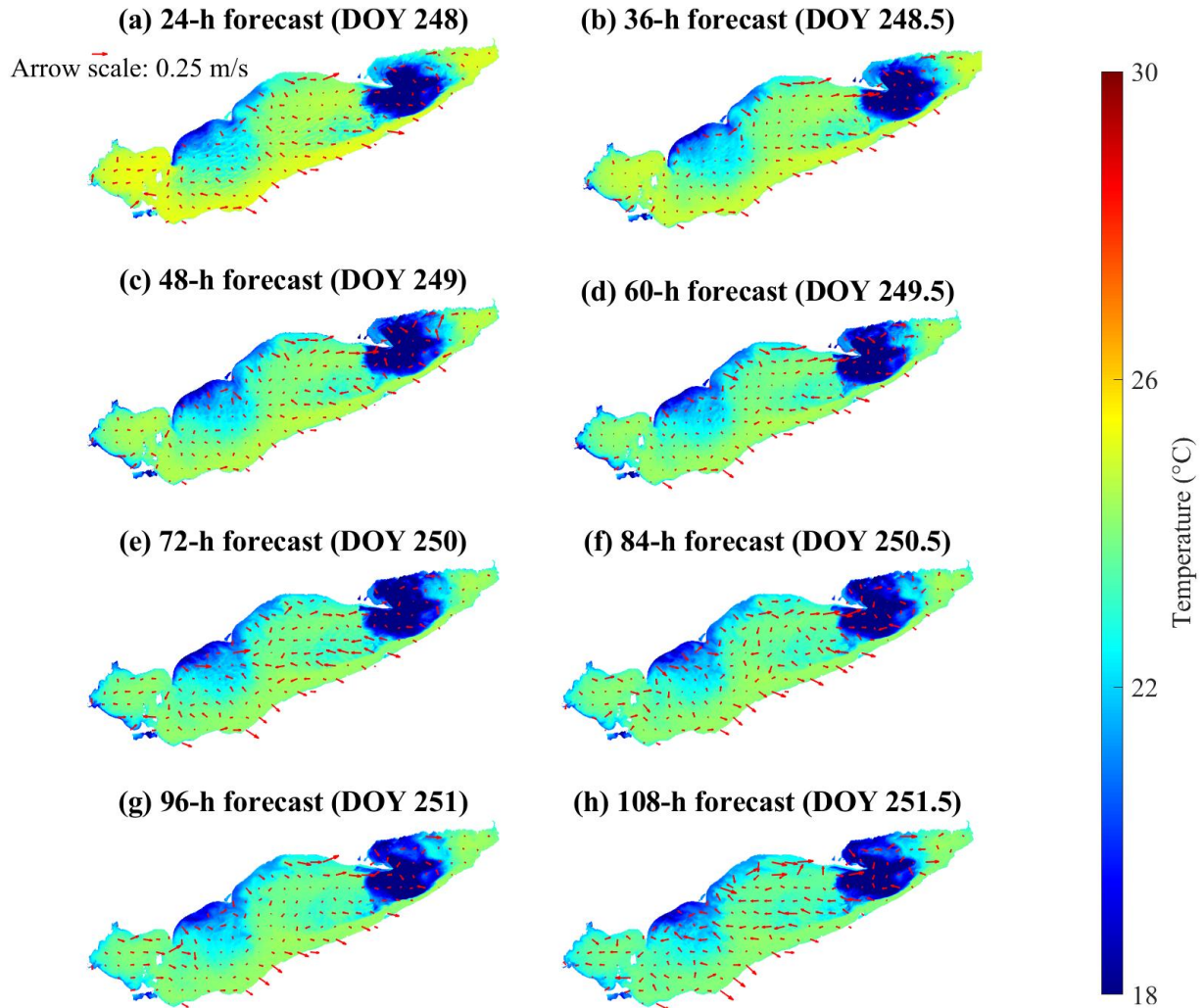
337 The central basin of Lake Erie is vulnerable to hypoxia in summer from near-bed thermal stratification and the
 338 relatively large ratio of sediment area to hypolimnetic volume (Bouffard et al., 2013; Nakhaei et al., 2021).

339 Associated fish kill events (10s of thousands) are regularly reported, including an event on north shore of the central
 340 basin in the late summer of 2012, which was presumably was caused by up-welling of cold anoxic water from the
 341 hypolimnion (MOE, 2012; Rao et al., 2014). Similarly, 1000s of freshwater drum were killed in a rapid warming
 342 event (~5 °C /week) in the western basin in 2020 (<https://www.13abc.com/content/news/Hundreds-of-dead-fish->

343 [wash-up-in-Sandusky-Bay-571025541.html](https://www.epa.gov/wash-up-in-Sandusky-Bay-571025541.html)). Similarly, shoreward advection of hypoxic water, from up-welling or
344 internal waves also adversely affects source water quality at drinking water intakes (<https://epa.ohio.gov>), whereby
345 high Fe and Mn or low pH, associated with hypoxic water requires adjustment of treatment processes. This is a
346 particular issue along the Ohio coast of the central basin (Ruberg et al., 2008; Rowe et al., 2019).

347 The ability to predict these movements of hypolimnion water would aid management of both Lake Erie
348 fisheries and drinking water treatment. Here, we test the ability of the model to predict up-welling of cold bottom
349 water in the region where the fish kill was observed in 2012. On days 249-253, 2020 (Fig. 8) strong southwesterly
350 winds ($\sim 12 \text{ m s}^{-1}$; Fig. C2) were modelled and observed to create up-welling along the north shore, as expected
351 from Ekman drift of the surface layer (Jabbari et al., 2019). The upwelled cold hypolimnetic water is shown near the
352 coast of Erieau in the satellite observations and the 15 km resolution model (Fig. 8 a, b, e, f). The depth-averaged
353 water temperature and current circulation in the forecast shows up-welling to persist for several days (Fig. 11), with
354 cold hypolimnetic water accumulating along north shore and strong eastward currents along the northern shoreline
355 of the east-central basin. The up-welling region matched that shown in a 2013 hindcast simulation (Valipour et al.,
356 2019), revealing the hotspots of vertical transport of nutrients and anoxic hypolimnetic water.

357 Another up-welling event occurred near the Cleveland drinking water intake crib on days 167-170 (Fig. 9).
358 This event was accompanied by simultaneous $\sim 8 \text{ mg L}^{-1}$ oscillations in the observed dissolved oxygen concentration
359 (Fig. 9 c) at STN 45164 ($\sim 20 \text{ km}$ away from STN 45176), followed by the dissolved oxygen concentration
360 becoming locally hypoxic ($< 2 \text{ mg/L}$) for ~ 2 days. The COASTLINES model predicted this event (section 3.2.2),
361 which would have provided sufficient notice for drinking water plant operators to implement the additional
362 treatment required for hypoxic water (Rowe et al., 2019). Future work, using the coupled iWaterQuality
363 biogeochemical module (formerly CAEDYM) could extend COASTLINES to forecast water quality in Lake Erie
364 (León et al., 2011), including dissolved oxygen concentrations and formation of algae blooms (Bocaniov et al.,
365 2020).



366

367 **Fig. 11 Color maps showing the forecast depth-averaged temperature throughout the lake. The red arrows**
 368 **represent forecast depth-averaged currents. The model results are from the 240-h forecast model hot-started**
 369 **on day 247.**

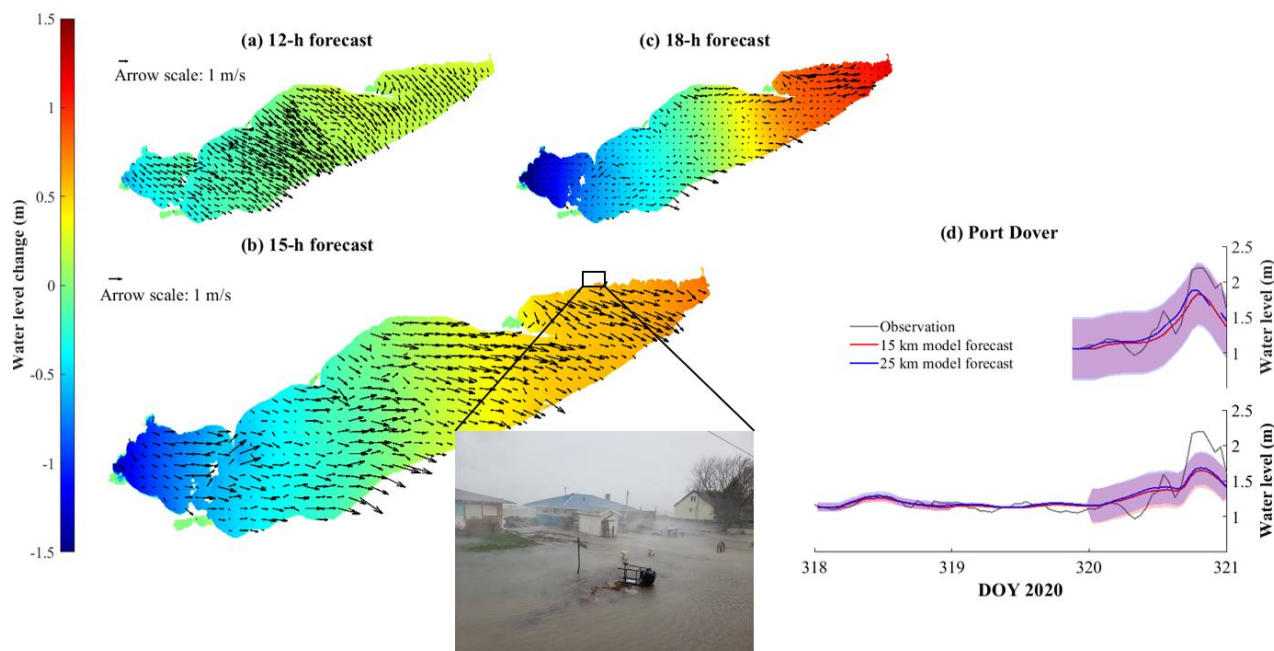
370 **4.2 Prediction of storm surge events for public safety**

371 Due to its shallowness and long fetch aligned with the predominant southwest winds (Hamblin, 1979), Lake Erie has
 372 the largest daily range of water level amongst the Great Lakes (Trebitz, 2006); these water level fluctuations are
 373 mainly due to storm surges and surface seiches (Mortimer, 1987). In every month of 2020, Lake Erie set new mean
 374 water level records (<https://www.tides.gc.ca/C&A/bulletin-eng.html>), causing the shoreline to be exposed to high
 375 risk from erosion and flooding and making the shoreline communities susceptible to costly damage and economic
 376 loss (e.g., <https://www.lowerthames-conservation.on.ca/flood-forecasting/flood-notice/>). Given the ability of
 377 COASTLINES to predict water level fluctuations induced by storm surges and seiches (Fig. 3, 5), we tested the
 378 ability of the model to act as a coastal flooding warning system. Due to the unpredictability and severity of water

379 level fluctuations in Lake Erie, there is currently a need to improve short-term water level forecasts and water level
 380 warning systems (Gronewold and Stow, 2014). This would assist early decision making during natural hazards
 381 (Gronewold and Rood, 2019).

382 We forecast the storm event on 15 Nov. 2020, which generated a wind-induced storm surge (~1-1.5 m) in
 383 the eastern basin with associated strong surface currents (Fig. 12). The inset image, taken during the event, shows
 384 the coastal flooding from this event. COASTLINES successfully predicted the high-water level phase at Port Dover
 385 72 hours in advance, but underestimated the water level increase by 0.5 m. The hot-start forecast 24 hours in
 386 advance was more accurate in predicting the water level prediction, with a difference <0.5 m from the observations
 387 (Fig. 12 d). Note that both forecasts missed the small (~0.5 m) seiche before the significant increase at the end of
 388 day 320, presumably due to the low temporal resolution of the meteorological forecast input or local topography
 389 near the gauge. The overall wind-induced tilt of the free surface was less from the 72 hours hot-start, relative to the
 390 24 hour hot start (Fig. E1), which predicted a larger local storm surge (Fig. 12d).

391 The impacts of coastal flooding could be improved by including simulation of wind-waves through
 392 enabling the coupled surface wave model SWAN (Booij et al., 1999) in AEM3D. Similarly coupled Delft3D-SWAN
 393 models have recently been applied in the development of a real-time predictive system for the coastal ocean and
 394 large estuaries (Rey and Mulligan, 2021).



395
 396 **Fig. 12** Color maps showing the water level change compared to Nov 15th 00h from (a) 12 h, (b) 15 h, and (c)
 397 18 h forecasts from 15 km resolution model. The black arrows are depth-averaged mean current fields. Panel
 398 (d) shows a comparison between forecast and observed water level at Port Dover. The upper panel shows the
 399 forecast hot-started on 15 Nov. 2020 (day 320), and the lower panel shows the forecast hot-started on 12 Nov.
 400 2020 (day 317). The shaded region indicates the confidence interval. The inset image (extracted from a footage
 401 by J. Homewood from Lower Thames Valley Conservation Authority) shows the flooding induced by the
 402 dramatic water level increase during this event. The two cottages shown in the images were destroyed later in
 403 the afternoon.

404 4.3 Bias and uncertainty

405 The AEM3D model (formerly ELCOM) employed in COASTLINES has shown skill in temperature hindcasts in the
406 Great Lakes with RMSD $\sim 0.9 - 3$ °C in Lake Erie (Liu et al., 2014; Oveisy et al., 2012) and $1.5 - 1.9$ °C in Lake
407 Ontario (Paturi et al., 2012). Similarly, the 24-h COASTLINES forecast predicted water temperatures with an
408 average s-RMSD and t-RMSD < 2 °C at the surface (Table 2). Therefore, the forecasts are within ~ 1 °C RMSD in
409 comparison to hindcasts, showing sufficient model skill for predictive simulations to aid lake management (e.g.,
410 movements of hypoxic water, fish thermal habitat, etc.). The accuracy of the COASTLINES forecasts may result
411 from the high spatial resolution and coverage of meteorological forecast compensating for the inherent inaccuracies
412 in the weather forecast data. Errors in forcing data may be compensated for using data assimilation (Baracchini et
413 al., 2020b). In the hindcast models, Liu et al. (2014) applied uniform Lake Erie meteorological forcing over 4 zones
414 and Valipour et al. (2019) utilized 6 zones, each spanning ~ 100 km. These included land-based observations, when
415 there was no available lake buoy data, which induces error, especially in large shallow lakes (Hamblin, 1987). The
416 comparatively high-resolution GDPS meteorological forecast was four to five times higher in horizontal resolution
417 than used in the hindcast simulations, improving the representation of regional meteorological and climatological
418 conditions.

419 Compared to other operational lake forecast systems, the 240-h COASTLINES forecast is longer (e.g.,
420 GLCFS forecasts 120 hours and meteolakes.ch forecasts 108 hours) and is the only one forced with open-access
421 meteorological data that has global coverage. The GLCFS provided 48-h water level forecasts with RMSD ~ 0.12 m
422 at the Buffalo gauge and ~ 0.14 m at the Toledo gauge, corresponding to RE $\sim 60\%$ and 51% , respectively (O'connor
423 et al., 1999; Trebitz, 2006); using the older 4 km grid Princeton Ocean Model implementation, as opposed to the
424 newer unstructured grid FVCOM GLCFS. COASTLINES gives better 48-h water level forecast performance (RE \sim
425 40%) at six gauge stations. For temperature, benefitting from a smaller domain, finer resolution meteorological
426 input (~ 2.2 km) and data assimilation, the 4.5-day lake surface temperature predicted by meteolakes.ch has a RMSD
427 $= 0.8$ °C (Baracchini et al., 2020b), whereas COASTLINES predicted the 120-h (5 d) lake surface temperature with
428 RMSD ~ 1.7 °C. COASTLINES also outperforms 1D climatological hindcasts (e.g., Freshwater Lake (FLake)),
429 with $2 - 4$ °C RMSD over a 120-h lake surface temperature forecast (Lv et al., 2019; Gu et al., 2015) and has similar
430 error to the 3D Princeton Ocean Model (Kelley et al., 1998), with $0.6 - 0.9$ °C mean absolute error in the 36-h lake
431 surface temperature forecast at station 45005.

432 The uncertainty and bias in the COASTLINES forecast results from error induced by the initial conditions
433 at each hot-start, error in the meteorological forecasts and error in the numerical methods. These errors could be
434 reduced by improving model calibration through data assimilation. For example, Baracchini et al. (2020b) reduced
435 the RMSE temperature simulation of Lake Geneva from ~ 2 °C to ~ 1 °C by employing a sequential data
436 assimilation routine; this would correspond to a $< 5\%$ improvement in simulation of Lake Erie summer surface
437 temperature. In AEM3D, sequential data assimilation could be implemented through modification of the restart files
438 (aem3d_restart_v3_type.f90); however this is beyond the scope of the present study. Before implementing data
439 assimilation in our system, the limitations of such a scheme must be considered: (i) As we are performing forecasts,
440 not hindcasts, we are unable to assimilate observations during model runtime (e.g., as done in the NCEP North

441 ~~American Regional Reanalysis: NARR); (ii) Sequential assimilation could be employed to nudge the initial~~
442 ~~conditions for the 24-h runs with real-time observed data. This could be achieved by modifying the binary AEM3D~~
443 ~~restart files using model-specific read/write statements in our Python workflow (e.g., from~~
444 ~~aem3d_restart_v3_type.f90), followed by smoothing (e.g., with a Kalman filter).~~ Future work will focus on adding
445 real-time model calibration (e.g., Gaudard et al. (2019)), which is not presently included in the COASTLINES
446 forecast workflow. For example, Baracchini et al. (2020a) employed OpenDA as a black-box wrapper to calibrate
447 DELFT3D for Lake Geneva.

448 The errors induced by hot-starting were shown to be negligible (Fig. 4, 6, 7 (a, b), Fig. A1). However,
449 uncertainty from boundary conditions, especially the meteorological forcing, may introduce error. The 23 to 31
450 meteorological zones from the forecast wind field provides spatial variability required to simulate the mean surface
451 circulation (Laval et al., 2003), water level (Treibitz, 2006), and thermocline motions (Valipour et al., 2015; Valipour
452 et al., 2019). However, the 3-h time interval between GDPS forecast dataset updates is much less than the 10-min
453 interval associated with meteorological data observed at lake-buoys (typically one to six) used to drive hindcasts
454 (e.g., León et al. (2005)) and so the coarse temporal resolution in GDPS forecast may alias temporal events, such as
455 wind gusts (Fig. C1). This is of particular concern in large shallow lakes, such as Lake Erie, where winds play the
456 dominant role in driving hydrodynamics. The rapid response of the water level to windstorms (Hamblin, 1987)
457 could result in the effects of aliasing and forecast error being passed to the water level, leading to the growth of RE
458 against forecast time (Fig. 3). The meteorological forecast from the 15 km and 25 km GDPS models did not show
459 discrepancies (Fig. C2-5) and the evaluation metrics indicate that forecast results were largely insensitive to the
460 meteorological inputs in Lake Erie (Fig. 3, 7). However, the 15 km model better predicted the mesoscale upwelling
461 event (Fig. 8, 9, D2). The 24-h air temperature and wind speed forecasts had ~ 1.5 °C and ~ 2 m s⁻¹ RMSD,
462 respectively. However, bias in the 240-h forecast increases with forecast time (Buehner et al., 2015). The 168-h
463 forecast meteorological data overestimated wind speeds by up to 10 m s⁻¹ (Fig. C4), and bias in the air temperature
464 forecast (Fig. C5) may cause the consistent warm bias (up to 3°C) in forecast lake surface temperature (Fig. 8).
465 These errors may be corrected through real-time calibration using data assimilation (Baracchini et al., 2020a, b). The
466 growing bias in air temperature, with forecast time, does not affect the lake surface temperature (Fig. 7), presumably
467 owing to the buffer effect of surface mixing layer (Schertzer et al., 1987).

468 Neglecting the inflows and outflows in the predictive simulation could induce bias in the forecast. The
469 overestimation of water level fluctuation range near Bar Point (Fig. 4f) may result from neglecting the large Detroit
470 River inflow, which regulates the seiche magnitude. The inflows also adjust more rapidly to air temperatures
471 compared to deep lake waters. Thus, the up to 2 °C cold bias in coastal regions of the western basin (Fig. 8 m-t, Fig.
472 D2) could be induced by neglecting the heated flux from two major inflows (i.e., Detroit River and Maumee River)
473 of Lake Erie.

474 In addition to inaccuracy in initial and boundary conditions, the discrepancies in simulating temperature
475 profiles forecast may result from numerical diffusion arising due to the discrete nature of the vertical and horizontal
476 grids. The simulated thermocline depth is overestimated (Fig. 9, 10), as occurred in applications of ELCOM with
477 both higher (Nakhaei et al., 2019) and lower resolution (Paturi et al., 2012). COASTLINES has the potential to

478 predictively simulate mesoscale physical processes, such as Kelvin waves (Bouffard and Lemmin, 2013) and
479 nearshore-offshore exchange (Valipour et al., 2019); however, model performance is poor in nearshore areas, where
480 topographic features remain poorly resolved.

481 5 Conclusions

482 We developed an operational forecast system COASTLINES, using the Windows Task Scheduler, Python-based
483 data scrapping/formatting, and MATLAB data processing scripts, to automate application of a black-box
484 hydrodynamic driver (AEM3D) to Lake Erie as an operational forecast tool. The resulting real-time and predictive
485 lake modelling system used meteorological forecasts to generate 240-h forecasts of the lake surface level and 3D
486 temperature and current fields on a 500 m × 500 m (horizontal) × ~ 1 m (vertical) grid, compares model output with
487 near real time observations and publishes the model output on a web-based platform.

488 The favorable agreement between forecast model results and observed physical variables (e.g., water level
489 RE ~ 40 % and temperature t-RMSD and s-RMSD < 2 °C) in Lake Erie demonstrates the ability of the forecast
490 system to make predictions of hydrodynamic processes on time horizons up to 240-h that are as accurate as
491 traditional hindcast simulations using directly observed meteorological forcing. This enables the near real-time
492 updates to the web platform to be used as a communication tool that rapidly disseminate forecast results to managers
493 and stakeholders. Examples include >24-h prediction of: (i) up- and down-welling events leading to fish kills; (ii)
494 up-welling events transporting hypoxic water to a drinking water intake; and (iii) coastal flooding events from storm
495 surges.

496 This operational system shows the feasibility of applying freely available meteorological forecasts (e.g.,
497 GDPS, HRRR), in situ buoy data and satellite images to drive and validate any computational lake model (e.g.,
498 AEM3D, DELFT3D, GLM), without modifying the source code. The global coverage of the weather model allows
499 generalization of model application to and lake or coastal domain. To facilitate further development of open-access
500 predictive modelling systems, agencies are encouraged to share model validation observations, in real-time, through
501 organizations such as GLEON (www.gleon.org) and GLOS (www.glos.us). This will enable extension of
502 COASTLINES to include prediction of the physical-biogeochemical variables that drive sediment transport,
503 hypoxia, and harmful algal blooms.

504

505 Code and data availability.

506 The observed data and meteorological forcing used in this study is openly accessible online as cited in the text. The
507 COASTLINES model output is archived on the server and can be obtained by contacting the corresponding author.
508 The Python and MATLAB scripts as well as the timeline set in Windows Task Scheduler are archived in the
509 Scholars Portal Dataverse (<https://doi.org/10.5683/SP2/VTN7WC>, Lin, 2021). The AEM3D executable was used as
510 a black box hydrodynamic transport code. The executable used in COASTLINES is available for a nominal license
511 fee from from Hydronumerics (<https://www.hydronumerics.com.au/>). The AEM3D source code was not modified
512 in this application but is available with permission from Hydronumerics.

513 **Author contributions.**

514 The concept of the COASTLINES workflow was designed by LB, SL, SS, and RM, and SL carried them out. SL
515 developed the model code and performed the simulations. All authors contributed to the validation of the model and
516 interpretation of the results. SL wrote the manuscript with contributions from LB, SS, and RM.

517 **Acknowledgements.**

518 This project was funded by the Dean's Research Fund from the Faculty of Engineering and Applied Science at
519 Queen's University. Computational support was provided by Alexander Rey and FEAS-ITS. LB thanks Damien
520 Bouffard for discussions during visits to EAWAG, which inspired this research. James Homewood, from the Lower
521 Thames Valley Conservation Authority (LTVCA) providing footages of the storm event on Nov. 15th, 2020.

522 **Reference**

- 523 Anderson, E. J., Fujisaki-Manome, A., Kessler, J., Lang, G. A., Chu, P. Y., Kelly, J. G. W., Chen, Y., and Wang, J.:
524 Ice forecasting in the next-generation Great Lakes Operational Forecast System (GLOFS), *J. Mar. Sci. Eng.*, 6,
525 10.3390/jmse6040123, 2018.
- 526 Antenucci, J., and Imerito, A.: The CWR dynamic reservoir simulation model DYRESM, Science Manual, The
527 University of Western Australia, Perth, Australia, 2000.
- 528 Baracchini, T., Hummel, S., Verlaan, M., Cimatoribus, A., Wüest, A., and Bouffard, D.: An automated calibration
529 framework and open source tools for 3D lake hydrodynamic models, *Environmental Modelling & Software*, 134,
530 104787, 2020a.
- 531 Baracchini, T., Wüest, A., and Bouffard, D.: Meteolakes: An operational online three-dimensional forecasting
532 platform for lake hydrodynamics, *Water Res.*, 172, 10.1016/j.watres.2020.115529, 2020b.
- 533 Beletsky, D., Hawley, N., Rao, Y. R., Vanderploeg, H. A., Beletsky, R., Schwab, D. J., and Ruberg, S. A.: Summer
534 thermal structure and anticyclonic circulation of Lake Erie., *Geophys. Res. Lett.*, 39, 10.1029/2012GL051002, 2012.
- 535 Bocaniov, S. A., and Scavia, D.: Temporal and spatial dynamics of large lake hypoxia: Integrating statistical and
536 three-dimensional dynamic models to enhance lake management criteria, *Water Resour. Res.*, 52, 4247-4263,
537 10.1002/2015WR018170, 2016.
- 538 Bocaniov, S. A., Lamb, K. G., Liu, W., Rao, Y. R., and Smith, R. E.: High sensitivity of lake hypoxia to air
539 temperatures, winds, and nutrient loading: Insights from a 3-D lake model, *Water Resources Research*, 56,
540 e2019WR027040, 2020.
- 541 Boegman, L., Loewen, M. R., Hamblin, P., and Culver, D.: Application of a two-dimensional hydrodynamic
542 reservoir model to Lake Erie, *Canadian Journal of Fisheries and Aquatic Sciences*, 58, 858-869, 2001.
- 543 Boegman, L., Loewen, M., Hamblin, P. F., and A., C. D.: Vertical mixing and weak stratification over zebra mussel
544 colonies in western Lake Erie, *Limnol. Oceanogr.*, 53, 1093-1110, 10.4319/lo.2008.53.3.1093, 2008.
- 545 Booij, N., Ris, R. C., and Holthuijsen, L. H.: A third-generation wave model for coastal regions 1. Model description
546 and validation *J. Geophys. Res. Oceans*, 104, 7649-7666, 10.1029/98JC02622, 1999.
- 547 Bouffard, D., Boegman, L., and Rao, Y. R.: Poincaré wave-induced mixing in a large lake, *Limnology and
548 oceanography*, 57, 1201-1216, 2012.
- 549 Bouffard, D., Ackerman, J. D., and Boegman, L.: Factors affecting the development and dynamics of hypoxia in a
550 large shallow stratified lake: hourly to seasonal patterns, *Water Resources Research*, 49, 2380-2394, 2013.
- 551 Bouffard, D., and Lemmin, U.: Kelvin waves in Lake Geneva, *J. Great Lakes Res.*, 39, 637-645,
552 10.1016/j.jglr.2013.09.005, 2013.
- 553 Bouffard, D., Boegman, L., Ackerman, J. D., Valipour, R., and Rao, Y. R.: Near-inertial wave driven dissolved
554 oxygen transfer through the thermocline of a large lake, *J. Great Lakes Res.*, 40, 300-307,
555 10.1016/j.jglr.2014.03.014, 2014.
- 556 Brookes, J. D., and Carey, C. C.: Resilience to blooms, *Science*, 334, 46-47, 10.1126/science.1207349, 2011.
- 557 Buehner, M., McTaggart-Cowan, R., Beaulne, A., Charette, C., Garand, L., Heilliette, S., Lapalme, E., Laroche, S.,
558 Macpherson, S. R., Morneau, J., and Zadra, A.: Implementation of deterministic weather forecasting systems based
559 on ensemble-variational data assimilation at Environment Canada. Part I: the global system, *Mon. Wea. Rev.*, 143,
560 2532-2559, 10.1175/MWR-D-14-00354.1, 2015.
- 561 Caramatti, I., Peeters, F., Hamilton, D., and Hofmann, H.: Modelling inter-annual and spatial variability of ice cover
562 in a temperate lake with complex morphology, *Hydrol. Process.*, 34, 691-704, 10.1002/hyp.13618, 2019.
- 563 Casulli, V., and Cheng, R.: Semi-implicit finite difference methods for three-dimensional shallow water flow. , *Int.
564 J. Numer. Methods Fluids* 15, 629-648, 10.1002/fld.1650150602 1992.
- 565 Chen, C., Beardsley, R. C., Cowles, G., Qi, J., Lai, Z., Gao, G., Stuebe, D., Xu, Q., Xue, P., Ge, J., Ji, R., Tian, R.,
566 Huang, H., Wu, L., and Lin, H.: An unstructured grid, finite-volume community ocean model FVCOM user manual,
567 SMASST/UMASSD Tech. Rep. 11-1101, 373 pp., Dartmouth, Mass., 2012.
- 568 Chu, P. Y., Kelley, J. G. W., Mott, G. V., Zhang, A., and Lang, G. A.: Development, implementation, and skill
569 assessment of the NOAA/NOS Great Lakes Operational Forecast System, *Ocean Dyn.* , 61, 1305-1316,
570 10.1007/s10236-011-0424-5, 2011.
- 571 Gaudard, A., Schwefel, R., Vinnå, L. R., Schmid, M., Wüest, A., and Bouffard, D.: Optimizing the parameterization
572 of deep mixing and internal seiches in one-dimensional hydrodynamic models: a case study with Simstrat v1.3,
573 *Geosci. Model Dev.*, 10, 3411-3423, 10.5194/gmd-10-3411-2017, 2017.
- 574 Gaudard, A., Vinnå, L. R., Bärenbold, F., Schmid, M., and Bouffard, D.: Toward an open-access of high-frequency
575 lake modelling and statistics data for scientists and practitioners. The case of Swiss Lakes using Simstrat v2.1,
576 *Geosci. Model Dev.*, 12, 3955-3974, 10.5194/gmd-2018-336, 2019.

577 Gronewold, A. D., and Rood, R. B.: Recent water level changes across Earth's largest lake system and implications
578 for future variability, *J. Great Lakes Res.*, 45, 1-3, 10.1016/j.jglr.2018.10.012, 2019.

579 Gu, H., Jin, J., Wu, Y., Ek, M. B., and Subin, Z. M.: Calibration and validation of lake surface temperature
580 simulations with the coupled WRF-lake model, *Climatic Change*, 129, 471-483, 2015.

581 Hamblin, P. F.: Great Lakes storm surge of April 6, 1979, *J. Great Lakes Res.*, 5, 312-315, 10.1016/S0380-
582 1330(79)72157-5, 1979.

583 Hamblin, P. F.: Meteorological forcing and water level fluctuations on Lake Erie, *J. Great Lakes Res.*, 13, 436-453,
584 10.1016/S0380-1330(87)71665-7, 1987.

585 Hecky, R. E., Smith, R. E. H., Barton, D. R., Guildford, S. J., Taylor, W. D., Charlton, M. N., and Howell, T.: The
586 nearshore phosphorus shunt: a consequence of ecosystem engineering by dreissenids in the Laurentian Great Lakes,
587 *Can. J. Fish. Aquat. Sci.*, 61, 1285-1293, 10.1139/F04-065, 2004.

588 Higgins, S. N., Hecky, R. E., and Guildford, S. J.: Environmental controls of cladophora growth dynamics in eastern
589 Lake Erie: Application of the Cladophora Growth Model (CGM), *J. Great Lakes Res.*, 32, 629-644, 10.3394/0380-
590 1330(2006)32[629:ECOCGD]2.0.CO;2, 2006.

591 Hipsey, M. R., Bruce, L. C., and Hamilton, D. P.: GLM - General Lake Model. Model overview and user
592 information, Technical Manual, The University of Western Australia, Perth, Australia., 2014.

593 Hodges, B. R., Imberger, J., Saggio, A., and Winters, K. B.: Modeling basin-scale internal waves in a stratified lake,
594 *Limnology and Oceanography*, 45, 1603-1620, 10.4319/lo.2000.45.7.1603, 2000.

595 Jabbari, A., Ackerman, J. D., Boegman, L., and Zhao, Y.: Episodic hypoxia in the western basin of Lake Erie,
596 *Limnology and Oceanography*, 64, 2220-2236, 2019.

597 Jabbari, A., Ackerman, J. D., Boegman, L., and Zhao, Y.: Increases in Great Lake winds and extreme events
598 facilitate interbasin coupling and reduce water quality in Lake Erie, *Scientific Reports*, 11, 5733, 10.1038/s41598-
599 021-84961-9, 2021.

600 Kelley, J. G. W., Hobgood, J. S., Bedford, K. W., and Schwab, D. J.: Generation of Three-Dimensional Lake Model
601 Forecasts for Lake Erie, *Weather and Forecasting*, 13, 659-687, 10.1175/1520-
602 0434(1998)013<0659:GOTDLM>2.0.CO;2, 1998.

603 Laval, B., Imberger, J., Hodges, B. R., and Stocker, R.: Modeling circulation in lakes: Spatial and temporal
604 variations, *Limnology and oceanography*, 48, 983-994, 2003.

605 León, L. F., Imberger, J., Smith, R. E. H., Hecky, R. E., Lam, D. C. L., and Schertzer, W. M.: Modeling as a tool for
606 nutrient management in Lake Erie: a hydrodynamics study, *J. Great Lakes Res.*, 31, 309-318, 10.1016/S0380-
607 1330(05)70323-3, 2005.

608 León, L. F., Smith, R. E. H., Hipsey, M. R., Bocaniov, S. A., Higgins, S. N., Hecky, R. E., Antenucci, J. P.,
609 Imberger, J. A., and Guildford, S. J.: Application of a 3D hydrodynamic-biological model for seasonal and spatial
610 dynamics of water quality and phytoplankton in Lake Erie, *J. Great Lakes Res.*, 37, 41-53,
611 10.1016/j.jglr.2010.12.007, 2011.

612 Leonard, B. P.: The ULTIMATE conservative difference scheme applied to unsteady one-dimensional advection.,
613 *Comp. Methods Appl. Mech. Eng.*, 88, 17-74, 1991.

614 Lesser, G. R., Roelvink, J. V., Van Kester, J. A. T. M., and Stelling, G. S.: Development and validation of a three-
615 dimensional morphological model. , *Coastal Engineering*, 51, 883-915, 10.1016/j.coastaleng.2004.07.014, 2004.

616 Liu, W., Bocaniov, S. A., Lamb, K. G., and Smith, R. E. H.: Three dimensional modeling of the effects of changes
617 in meteorological forcing on the thermal structure of Lake Erie, *J. Great Lakes Res.*, 40, 827-840,
618 10.1016/j.jglr.2014.08.002, 2014.

619 Loewen, M., Ackerman, J. D., and Hamblin, P. F.: Environmental implications of stratification and turbulent mixing
620 in a shallow lake basin, *Can. J. Fish. Aquat. Sci.* , 64, 43-57, 10.1139/F06-165, 2007.

621 Lv, Z., Zhang, S., Jin, J., Wu, Y., and Ek, M. B.: Coupling of a physically based lake model into the climate forecast
622 system to improve winter climate forecasts for the Great Lakes region, *Climate Dynamics*, 53, 6503-6517,
623 10.1007/s00382-019-04939-2, 2019.

624 Madani, M., Seth, R., León, L. F., Valipour, R., and McCrimmon, C.: Three dimensional modelling to assess
625 contributions of major tributaries to fecal microbial pollution of lake St. Clair and Sandpoint Beach, *J. Great Lakes
626 Res.*, 46, 159-179, 10.1016/j.jglr.2019.12.005, 2020.

627 Meyers, T., and Dale, R.: Predicting daily insolation with hourly cloud height and coverage, *Journal of Applied
628 Meteorology and Climatology*, 22, 537-545, 1983.

629 Michalak, A. a. M., Anderson, E. J., Beletsky, D., Boland, S., Bosch, N. S., Bridgeman, T. B., Chaffin, J. D., Cho,
630 K., Confesor, R., Daloğlu, I., DePinto, J. V., Evans, M. A., Fahnenstiel, G. L., He, L., Ho, J. C., Jenkins, L.,
631 Johengen, T. H., Kuo, K. C., LaPorte, E., Liu, X., McWilliams, M. R., Moore, M. R., Posselt, D. J., Richards, R. P.,
632 Scavia, D., Steiner, A. L., Verhamme, E., Wright, D. M., and Zagorski, M. A.: Record-setting algal bloom in Lake

633 Erie caused by agricultural and meteorological trends consistent with expected future conditions, *Proceedings of the*
634 *National Academy of Sciences*, 110, 6448-6452, 10.1073/pnas.1216006110, 2013.

635 MOE: Lake Erie fish kill incident on September 1, 2012. Summary Report. Ontario Ministry of the Environment
636 Southwestern Region 14 ((Available from Ontario Ministry of Environment)), 2012.

637 Mortimer, C. H.: Fifty Years of Physical Investigations and Related Limnological Studies on Lake Erie, 1928–1977,
638 *Journal of Great Lakes Research*, 13, 407-435, 10.1016/S0380-1330(87)71664-5, 1987.

639 Nakhaei, N., Boegman, L., Mehdizadeh, M., and Loewen, M.: Hydrodynamic modeling of Edmonton storm-water
640 ponds, *Environ. Fluid Mech.*, 19, 305-327, 10.1007/s10652-018-9625-5, 2019.

641 Nakhaei, N., Ackerman, J. D., Bouffard, D., Rao, Y. R., and Boegman, L.: Empirical modeling of hypolimnion and
642 sediment oxygen demand in temperate Canadian lakes, *Inland Waters*, 1-17, 2021.

643 O'Reilly, C. M., Sharma, S., Gray, D. K., Hampton, S. E., Read, J. S., and Rowley, R. J., et al.: Rapid and highly
644 variable warming of lake surface waters around the globe, *Geophys. Res. Lett.*, 42, 10773-10781,
645 10.1002/2015GL066235., 2015.

646 O'connor, W. P., Schwab, D. J., and Lang, G. A.: Forecast verification for Eta Model winds using Lake Erie storm
647 surge water levels, *Weather and forecasting*, 14, 119-133, 1999.

648 O'Neil, J. M., Davis, T. W., Burford, M. A., and Gobler, C. J.: The rise of harmful cyanobacteria blooms: The
649 potential roles of eutrophication and climate change, *Harmful Algae*, 14, 313-334, 10.1016/j.scitotenv.2011.02.001,
650 2012.

651 Oveisy, A., Boegman, L., and Imberger, J.: Three-dimensional simulation of lake and ice dynamics during winter,
652 *limnol. Oceanogr.*, 57, 42-57, 10.4319/lo.2012.57.1.0043, 2012.

653 Paerl, H. W., and Paul, V. J.: Climate change: Links to global expansion of harmful cyanobacteria, *Water Research*,
654 46, 1349-1363, 10.1016/j.watres.2011.08.002, 2012.

655 Paturi, S., Boegman, L., and Rao, Y. R.: Hydrodynamics of eastern Lake Ontario and the upper St. Lawrence River,
656 *J. Great Lakes Res.*, 38, 194-204, 10.1016/j.jglr.2011.09.008, 2012.

657 Rao, Y. R., and Murthy, C. R.: Coastal boundary layer characteristics during summer stratification in Lake Ontario.,
658 *J. Phys. Oceanogr.*, 31, 1088-1104, 10.1175/1520-0485(2001)031<1088:CBLCD>2.0.CO;2, 2001.

659 Rao, Y. R., Hawley, N., Charlton, M. N., and Schertzer, W. M.: Physical processes and hypoxia in the central basin
660 of Lake Erie, *Limnol. Oceanogr.*, 53, 2007-2020, 10.4319/lo.2008.53.5.2007, 2008.

661 Rao, Y. R., Howell, T., Watson, S. B., and Abernethy, S.: On hypoxia and fish kills along the north shore of Lake
662 Erie, *J. Great Lakes Res.*, 40, 187-191, 10.1016/j.jglr.2013.11.007, 2014.

663 Rey, A., and Mulligan, R. P.: Influence of Hurricane Wind Field Variability on RealTime Forecast Simulations of
664 the Coastal Environment, *J. Geophys. Res. Oceans*, 126, 10.1029/2020JC016489, 2021.

665 Rowe, M. D., Anderson, E. J., Beletsky, D., Stow, C. A., Moegling, S. D., and Chaffin, J. D., et al: Coastal
666 upwelling influences hypoxia spatial patterns and nearshore dynamics in Lake Erie., *J. Geophys. Res. Oceans*, 124,
667 10.1029/2019JC015192, 2019.

668 Ruberg, S. A., Guasp, E., Hawley, N., Muzzi, R. W., Brandt, S. B., and Vanderploeg, H. A., et al.: Societal benefits
669 of the Real-time Coastal Observation Network (ReCON): Implications for municipal drinking water quality., *Mar.*
670 *Technol. Soc. J.*, 42, 103-109, 10.4031/002533208786842471, 2008.

671 Saber, A., James, D. E., and Hannoun, I. A.: Effects of lake water level fluctuation due to drought and extreme
672 winter precipitation on mixing and water quality of an alpine lake, Case Study: Lake Arrowhead, California, *Sci.*
673 *Total Environ.*, 714, 10.1016/j.scitotenv.2020.136762, 2020.

674 Scavia, D., Allan, J. D., Arend, K. K., Bartell, S., Beletsky, D., Bosch, N. S., Brandt, S. B., Briland, R. D., Daloglu,
675 I., DePinto, J. V., Dolan, D. M., and Evans, M. A. e. a.: Assessing and addressing the re-eutrophication of Lake Erie:
676 Centralbasin hypoxia, *J. Great Lakes Res.*, 40, 226-246, 10.1016/j.jglr.2014.02.004, 2014.

677 Scavia, D., DePinto, J. V., and Bertani, I.: A multi-model approach to evaluating target phosphorus loads for Lake
678 Erie, *J. Great Lakes Res.*, 42, 1139-1150, 10.1016/j.jglr.2016.09.007, 2016.

679 Schertzer, W. M., Saylor, J. H., Boyce, F. M., Robertson, D. G., and Rosa, F.: Seasonal Thermal Cycle of Lake Erie,
680 *Journal of Great Lakes Research*, 13, 468-486, 10.1016/S0380-1330(87)71667-0, 1987.

681 Schwab, D. J., and Beletsky, D.: Propagation of kelvin waves along irregular coastlines in finite-difference models.,
682 *Adv. Water Resour.*, 22, 239-245, 10.1016/S0309-1708(98)00015-3, 1998.

683 Schwab, D. J., Leshkevich, G. A., and Muhr, G. C.: Automated Mapping of Surface Water Temperature in the Great
684 Lakes, *J. Great Lakes Res.*, 25, 468-481, 10.1016/S0380-1330(99)70755-0, 1999.

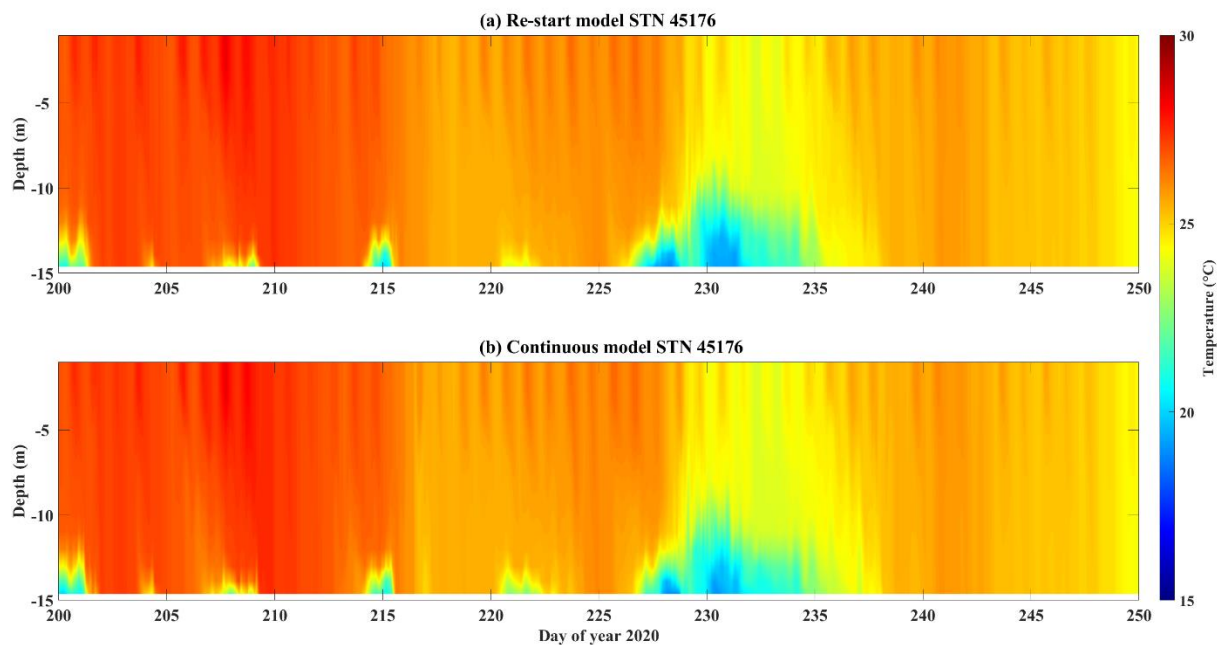
685 Trebitz, A. S.: Characterizing seiche and tide-driven daily water level fluctuations affecting coastal ecosystems of
686 the Great Lakes, *J. Great Lakes Res.*, 32, 102-116, 10.3394/0380-1330(2006)32[102:CSATDW]2.0.CO;2, 2006.

687 Valipour, R., Bouffard, D., Boegman, L., and Rao, Y. R.: Near-inertial waves in Lake Erie, *Limnol. Oceanogr.*, 60,
688 1522–1535, 10.1021/es301422r, 2015.

689 Valipour, R., Rao, Y. R., León, L. F., and Depew, D.: Nearshore-offshore exchanges in multi-basin coastal waters:
690 Observations and three-dimensional modeling in Lake Erie, *J. Great Lakes Res.*, 45, 50-60,
691 10.1016/j.jglr.2018.10.005, 2019.
692 Wang, Q., and Boegman, L.: Multi-Year Simulation of Western Lake Erie Hydrodynamics and Biogeochemistry to
693 Evaluate Nutrient Management Scenarios, *Sustainability*, 13, 7516, 2021.
694 Watson, S. B., Miller, C., Arhonditsis, G., Boyer, G. L., and al, e.: The re-eutrophication of Lake Erie: Harmful algal
695 blooms and hypoxia, *Harmful Algae*, 56, 44-66, 10.1016/j.hal.2016.04.010, 2016.
696 Woolway, R. I., and Merchant, C. J.: Worldwide alteration of lake mixing regimes in response to climate change.,
697 *Nat. Geosci.*, 12, 271-276, 10.1038/s41561-019-0322-x, 2019.
698 Woolway, R. I., Kraemer, B. M., and Lenters, J. D., et al.: Global lake responses to climate change, *Nat Rev Earth*
699 *Environ*, 10.1038/s43017-020-0067-5, 2020.

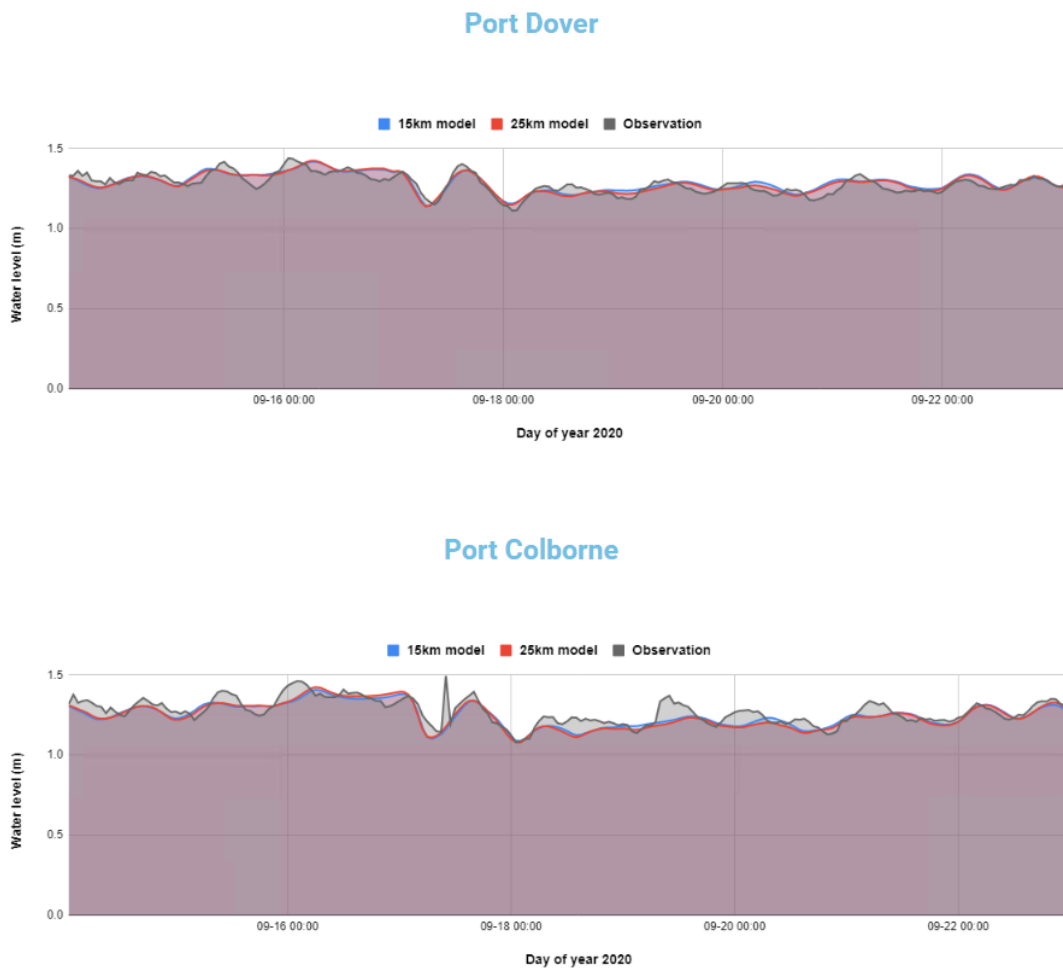
700

701 **Appendix A: Comparison of 24 h model run with re-start files and model run with continuous files.**



702 **Fig. A1 Temperature profile comparison between (a) stitched 24 h model run with re-start files, and (b) model**
703 **run with continuous input files.**
704

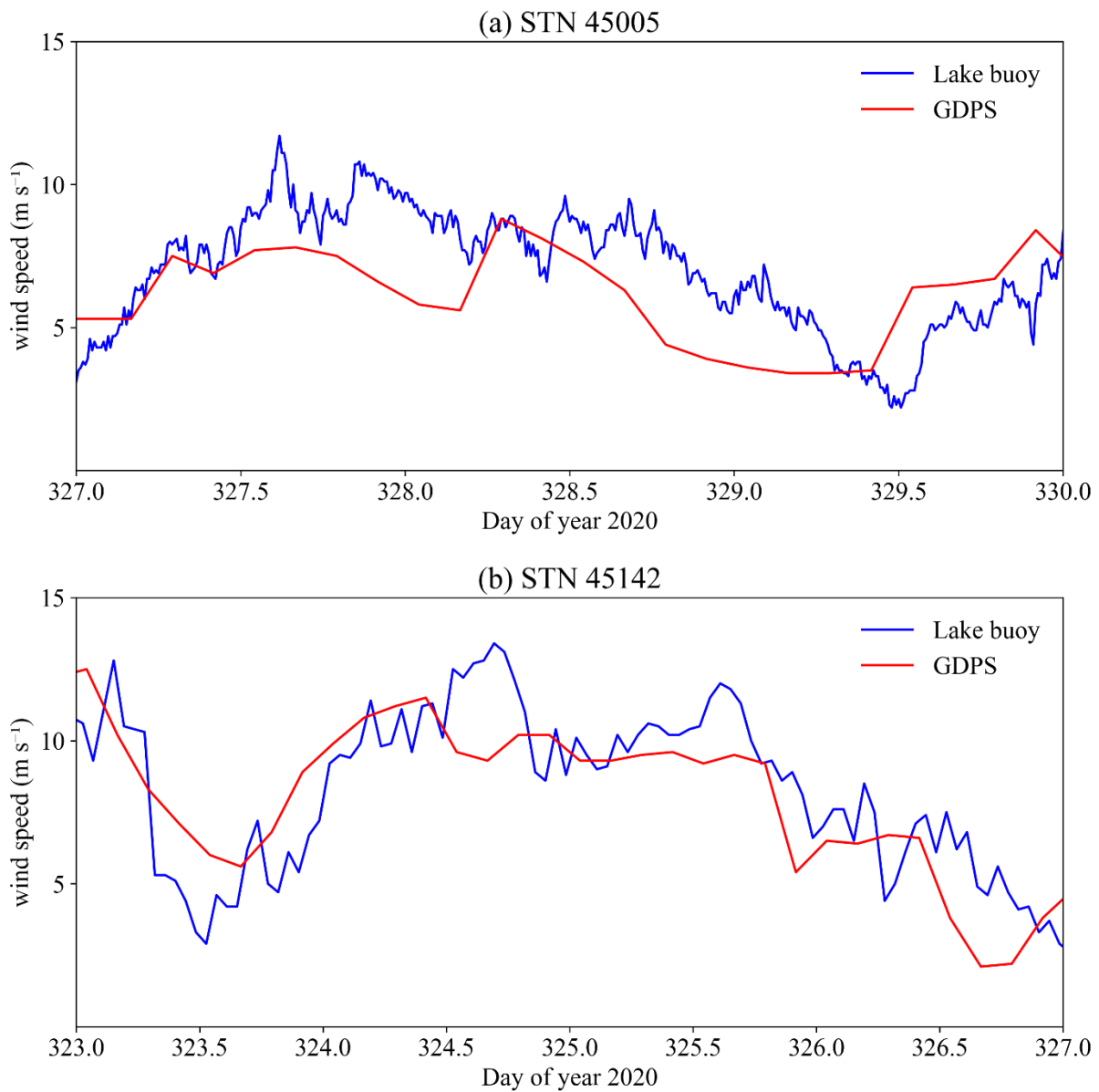
705



707

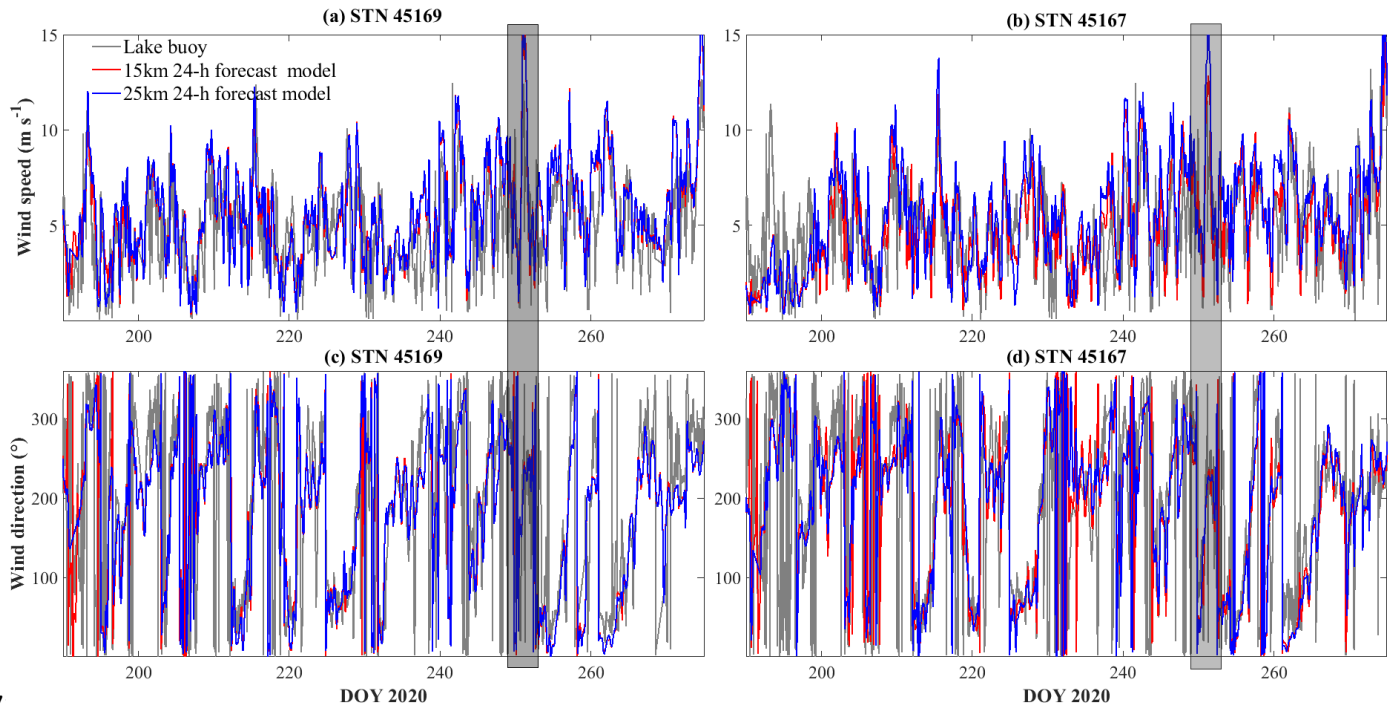
708 Fig. B1 Snapshot of water level forecast validation web page displayed on COASTLINES online platform:
709 <https://coastlines.engineering.queensu.ca/erie/water-level-forecast>. Status on Sep 23rd, 2020.

710



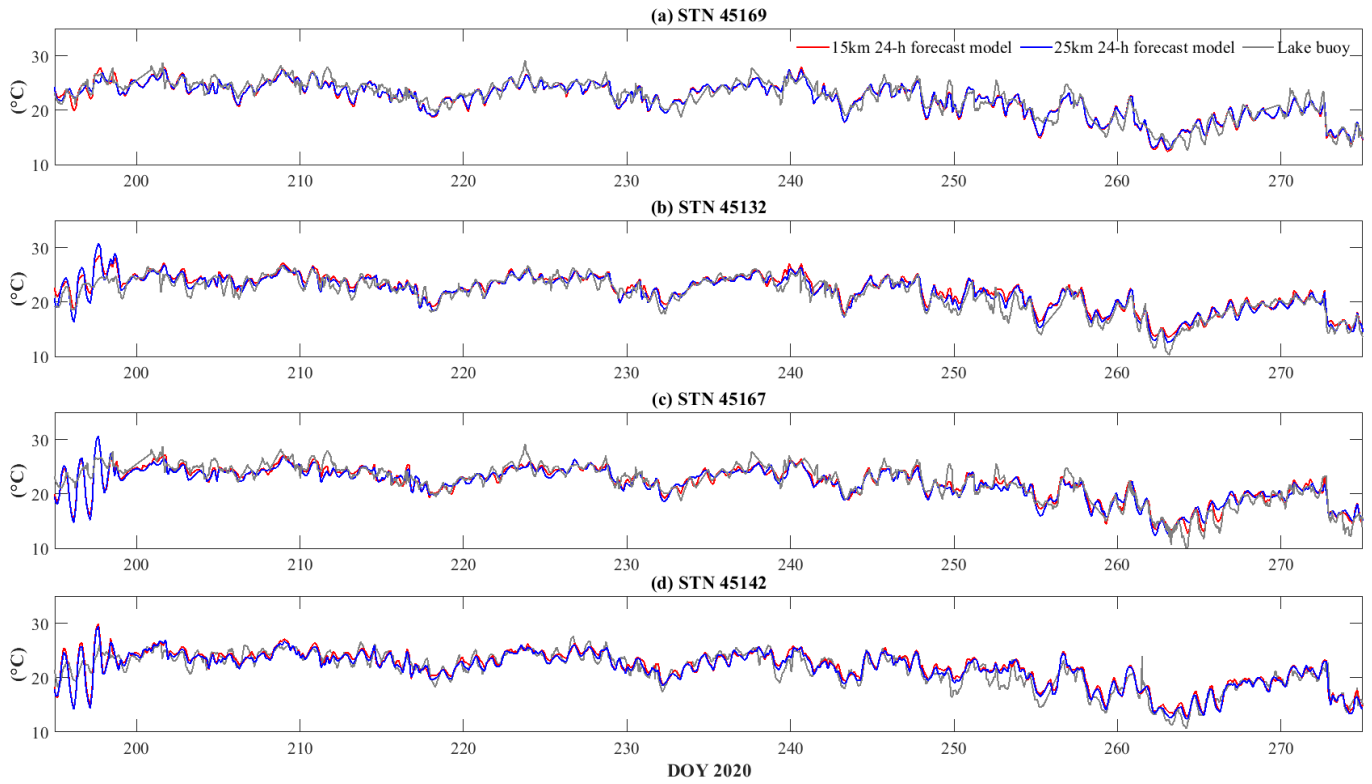
712

713 Fig. C1 Comparisons of stitched GDPS wind forecast with 3 h delivery interval and lake buoy measured wind
714 speed at (a) station 45005 (10 min sampling interval), and (b) station 45142 (1 h sampling interval). The wind
715 gusts on day 327 at station 45005 and day 324 at station 45142 were missed by wind forecast.



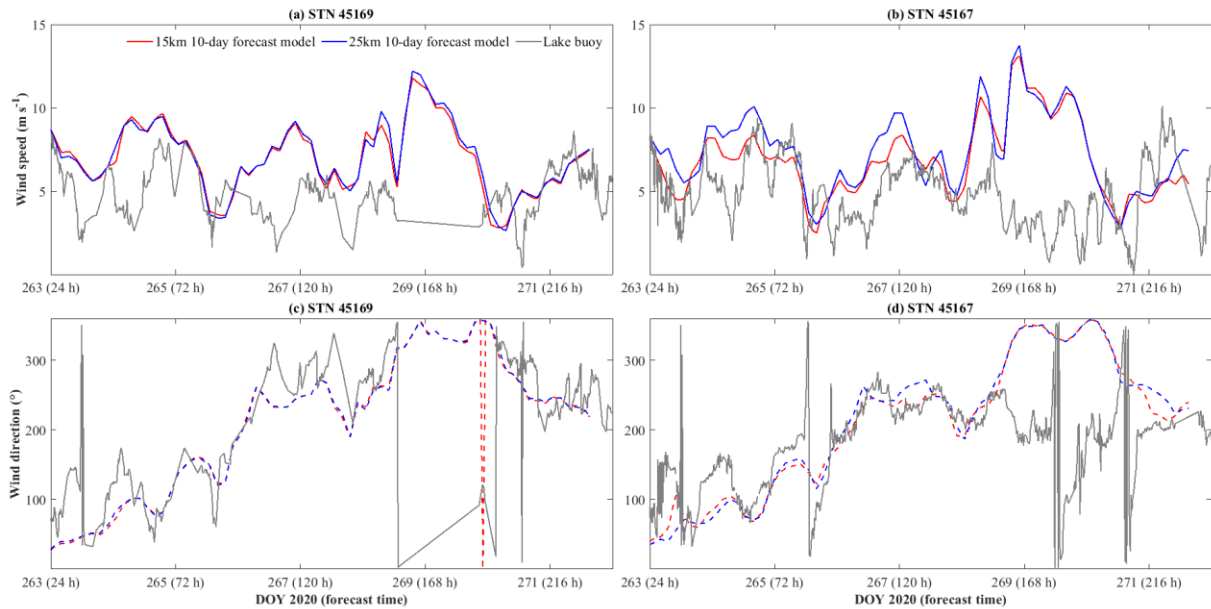
7

717 **Fig. C2 Comparisons of 24-h meteorological forecast and lake buoy observations of wind speed (a, b) and**
 718 **wind direction (c, d). The gray rectangle indicates the storm that led to up-welling along northern shoreline on days**
 719 **248-253.**



7.

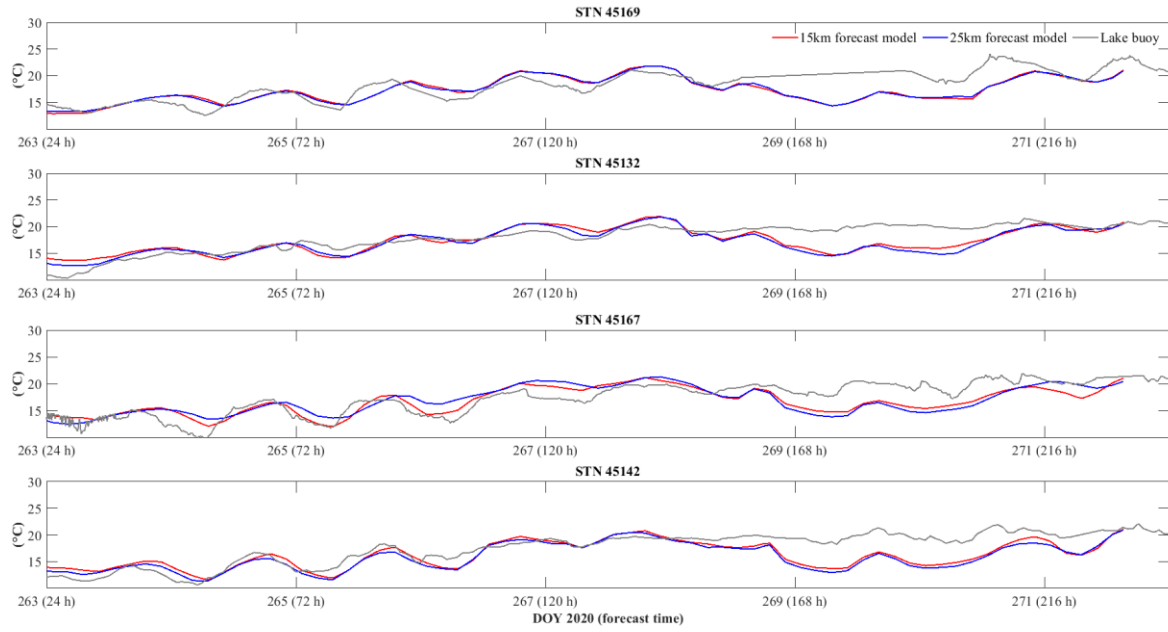
721 **Fig. C3 Comparisons of 24-h air temperature forecast and lake buoy observations of air temperature.**



722

723 **Fig. C4 Comparisons of 240-h meteorological forecast and lake buoy observations of wind speed (a, b) and wind**
 724 **direction (c, d).**

725

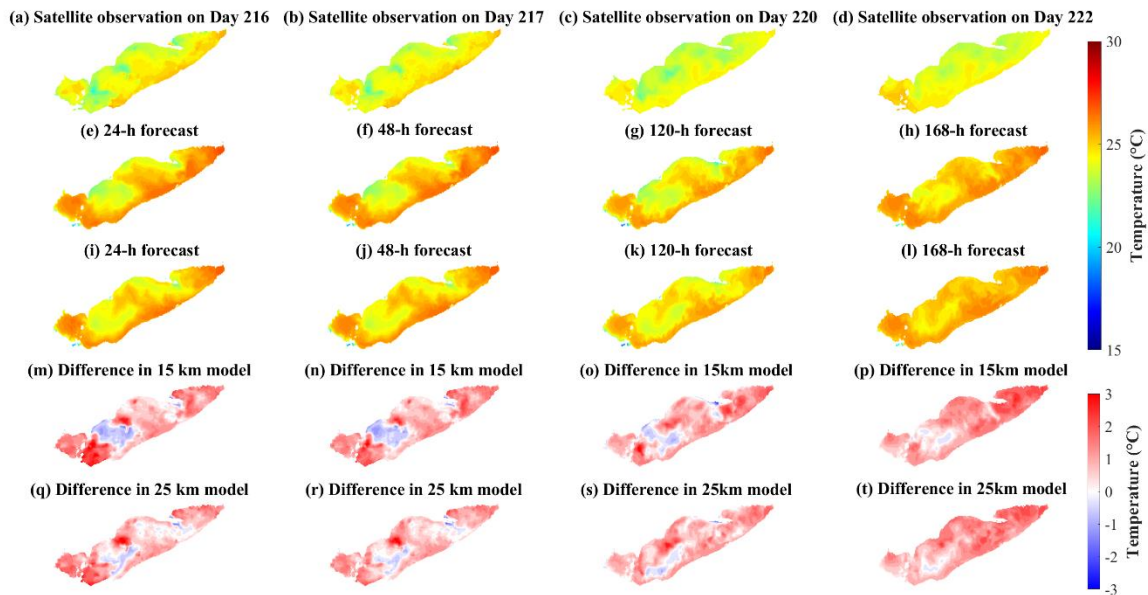


726

727 **Fig. C5 Comparisons of 240-h air temperature forecast and lake buoy observations.**

728 **Appendix D: Temperature validation against satellite observations**

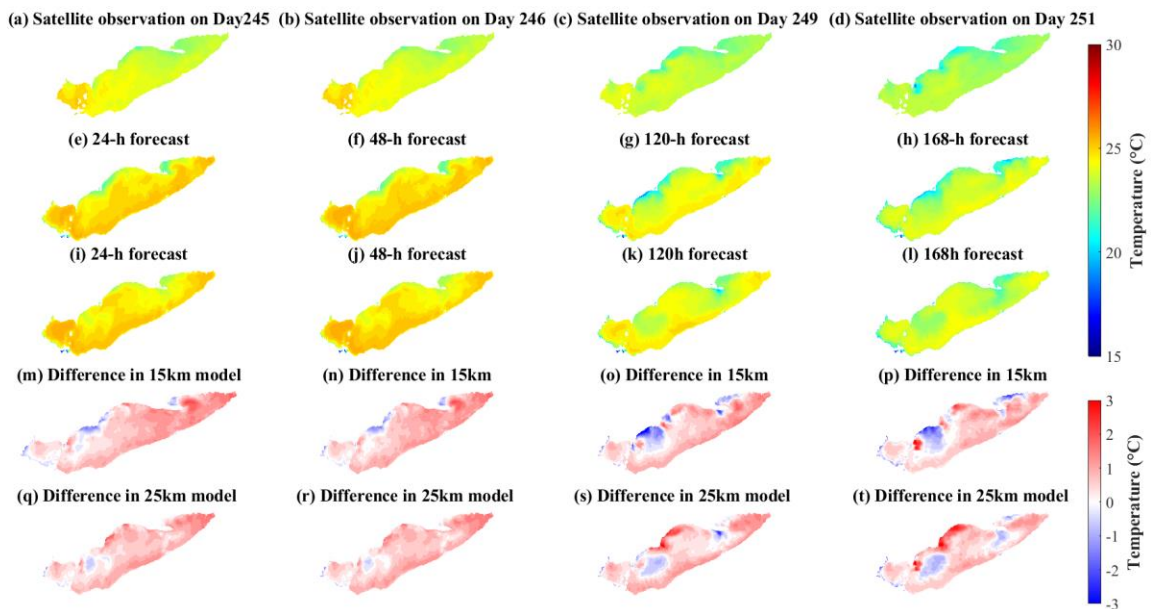
729



730

731 **Fig. D1** comparisons of (a-d) satellite observations, (e-h) 15 km model 240-h forecast, and (i-l) 25 km model
 732 240-h forecast during summer. The models were hot-started on Day 215. The difference between observations
 733 and models are shown in (m-t).

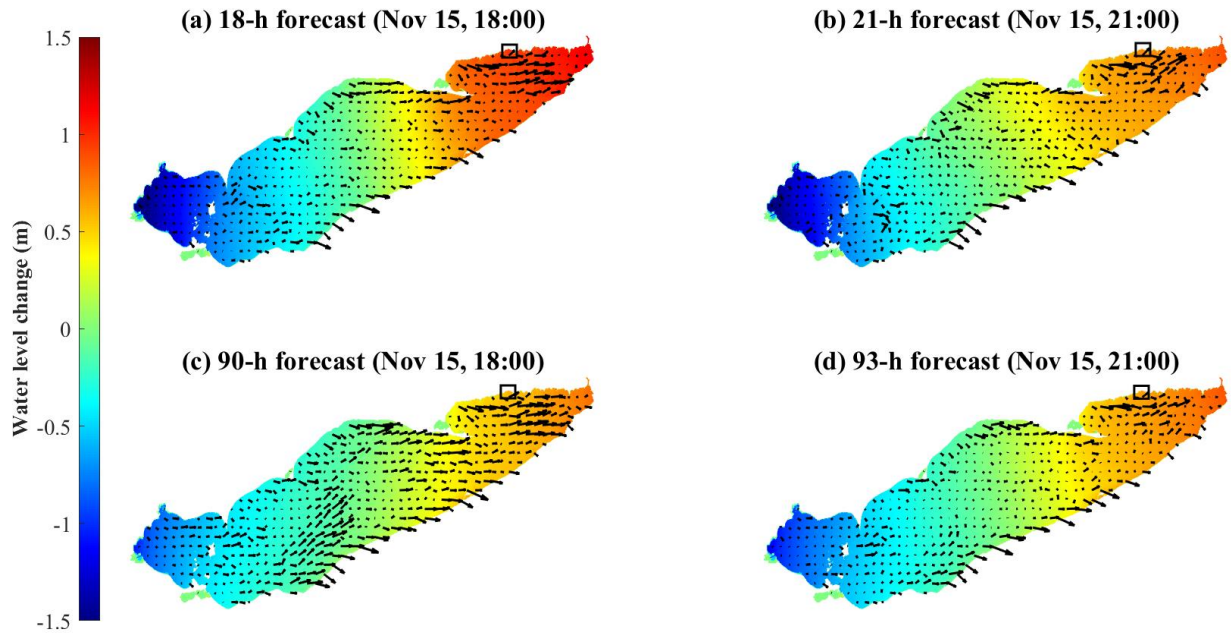
734



735

736 Fig. D2 comparisons of (a-d) satellite observations, (e-h) 15 km model 240-h forecast, and (i-l) 25 km model
737 240-h forecast during late summer. The models were hot-started on Day 244. The difference between
738 observations and models are shown in (m-t).

739 Appendix E: Water level change during windstorm on Nov 15th, 2020



740
741 Fig. E1 Spatial distribution of water level change from forecasts hot-started on Nov 15th (a, b) and Nov 12th
742 (c, d). The water level at Nov 15th 00:00 is the reference level. The black arrows are depth-averaged mean
743 current fields. The black squares in the upper right corners of each map indicate the location of Port Dover
744 (Fig. 12d).
745
746